

Complex Chemistry in Star-Forming Regions: An Expanded Gas-Grain Warm-up Chemical Model

Robin T. Garrod

Max-Planck-Institut für Radioastronomie, Auf dem Hügel 69, Bonn, 53121, Germany

rgarrod@mpifr-bonn.mpg.de

Susanna L. Widicus Weaver

Departments of Chemistry and Astronomy, University of Illinois at Urbana-Champaign, Urbana, IL 61801

slww@uiuc.edu

and

Eric Herbst

Departments of Physics, Chemistry and Astronomy, The Ohio State University, Columbus, OH 43210

ABSTRACT

Gas-phase processes were long thought to be the key formation mechanisms for complex organic molecules in star-forming regions. However, recent experimental and theoretical evidence has cast doubt on the efficiency of such processes. Grain-surface chemistry is frequently invoked as a solution, but until now there have been no quantitative models taking into account both the high degree of chemical complexity and the evolving physical conditions of star-forming regions. Here, we introduce a new gas-grain chemical network, wherein a wide array of complex species may be formed by reactions involving radicals. The radicals we consider (H, OH, CO, HCO, CH₃, CH₃O, CH₂OH, NH and NH₂) are produced primarily by cosmic ray-induced photodissociation of the granular ices formed during the colder, earlier stages of evolution. The gradual warm-up of the hot core is crucial to the formation of complex molecules, allowing the more strongly-bound radicals to become mobile on grain surfaces. This type of chemistry is capable of reproducing the high degree of complexity seen in Sgr B2(N), and can explain the observed abundances and temperatures of a variety of previously

detected complex organic molecules, including structural isomers. Many other complex species are predicted by this model, and several of these species may be detectable in hot cores. Differences in the chemistry of high- and low-mass star-formation are also addressed; greater chemical complexity is expected where evolution timescales are longer.

Subject headings: Astrochemistry, stars: formation, ISM: abundances, ISM: clouds, ISM: molecules, ISM: individual (Sagittarius B2(N))

1. Introduction

More than 140 molecules have been detected in the interstellar medium (ISM) or in circumstellar environments. Many of these species have been identified from their rotational emission spectra in hot cores – molecular regions that are spatially associated with high-mass star formation. Hot cores and their low-mass analogs, hot corinos, exhibit high temperatures (>100 K) and densities ($10^6 - 10^8 \text{ cm}^{-3}$), and are characterized by significant abundances of large, complex organic molecules including methanol (CH_3OH), formaldehyde (H_2CO), formic acid (HCOOH), methyl formate (HCOOCH_3), and dimethyl ether (CH_3OCH_3) (van Dishoeck & Blake 1998; Bottinelli et al. 2004a). The Galactic-Center hot-core source Sgr B2(N-LMH) exhibits the richest molecular inventory observed to date (e.g. Nummelin et al. 2000), showing spectral signatures of many additional complex organics, including acetone (CH_3COCH_3 , Snyder et al. 2002), ethylene glycol [$(\text{CH}_2\text{OH})_2$, Hollis et al. 2002], and glycolaldehyde [$\text{CH}_2(\text{OH})\text{CHO}$, Hollis et al. 2004]. The high degree of chemical complexity of these molecules, and the structural relationships between them, make their precise origins and formation mechanisms the subject of debate.

In molecular clouds, cold dust grains build up molecular ice mantles by the accretion and grain-surface hydrogenation of atoms and simple molecules from the gas phase. In regions of star formation, the gas and dust are heated to temperatures sufficient for these ices to evaporate. Infrared observations indicate the presence of icy grain mantles in the cold outer envelopes of protostellar objects (Gibb et al. 2004); these mantles are typically comprised mainly of H_2O , CO and CO_2 . Methanol, methane, formaldehyde, and ammonia are also observed in varying quantities, while the abundances of other, trace species are less well determined.

The evaporation of granular ices in the hot, dense regions fuels a rich network of gas-phase chemistry, to which the formation of many hot-core molecules has been attributed (e.g. Millar et al. 1991). Ion–molecule reactions, especially those involving evaporated formalde-

hyde and methanol, and the subsequent electronic recombination of protonated ions, are viewed as potential routes to forming complex hot-core species (Herbst et al. 1977; Charnley et al. 1995). However, recent investigations call into doubt the efficiency of such gas-phase routes. The experimental results of Geppert et al. (2006) suggest that formation of saturated complex molecules by electronic recombination of their protonated precursors is significantly less efficient than previously assumed; methanol and dimethyl ether are formed with respective efficiencies of $\sim 3\%$ and $\sim 5\%$ (W. Geppert, private comm.), implying similar inefficiency for other complex species. In addition, the quantum calculations of Horn et al. (2004) show that the ionic precursor of methyl formate cannot be formed in the gas phase at temperatures appropriate for hot cores. Grain-surface mechanisms may therefore be important to the formation of methyl formate, and perhaps many other observed hot-core molecules. The detection of complex molecules in hot corinos also points to grain-surface production, as gas-phase chemical timescales are greater than the transit time of the infalling gas in these sources (Schöier et al. 2002; Bottinelli et al. 2004a; Aikawa et al. 2007).

Garrod & Herbst (2006, hereafter GH06) used the OSU gas-grain chemical code to test grain-surface formation mechanisms for methyl formate, as well as dimethyl ether and formic acid. GH06 employed three heavy-radical combination reactions that were originally included in a large network developed by Allen & Robinson (1977) in the context of cold dark clouds. The surface radicals OH, HCO, CH₃ and CH₃O were allowed to combine to produce the three target molecules. Hollis & Churchwell (2001) pointed out the potential for complex-molecule formation from functional-group radicals such as these, suggesting a cold chemistry in which reactive functional groups are built up from accreted atoms. However, GH06 found that the complex molecules are formed predominantly at intermediate temperatures, when the grains become warm enough for heavy radicals to become mobile on grain surfaces, during the gradual warm-up of the hot core from 10 K to approximately 200 K. Further, the strongest source of heavy radicals was shown to be the cosmic ray-induced photodissociation of the icy mantles formed in the earlier cold collapse phase. Hence, in this scenario, the complex molecules are not themselves relics of the cold phase – but the ice composition preserved from that phase of evolution influences the chemistry by which they form at higher temperatures, as the hot core evolves.

The GH06 model demonstrated efficient means of forming complex molecules on grain surfaces, and served to highlight the complexity of gas-grain chemical interactions as temperatures evolve. It was shown that methyl formate almost certainly has a grain-surface origin, and may be produced in sufficient quantities to match observations, while dimethyl ether and formic acid may equally be formed in the gas phase or on grain surfaces, depending on the physical conditions and/or evolution timescale.

Here, we extend the reaction network to present a more complete study of hot-core chemistry, incorporating all thermodynamically-viable surface reactions between the radicals H, OH, HCO, CH₃, CH₃O, CH₂OH, NH and NH₂, as well as reactions with the resultant products. The radicals listed above may be produced by cosmic ray-induced photodissociation of the most abundant ice-mantle constituents. The majority of the new surface reactions form a subset of those suggested by Allen & Robinson (1977). We introduce 50 new grain surface-formed species, as well as a number of gas-phase species related to these, and we include gas-phase and grain-surface destruction mechanisms in keeping with other species in the network. The individual treatment of the structurally-isomeric radicals CH₃O and CH₂OH allows the differentiation of such important hot-core species as ethanol/dimethyl ether (C₂H₅OH, CH₃OCH₃), and glycolaldehyde/methyl formate/acetic acid [CH₂(OH)CHO, HCOOCH₃, CH₃COOH] – an important point, given the very different observational abundances of these molecules (Snyder et al. 2002).

We employ the physical model adopted by GH06 (based on Viti et al. 2004), which consists of an isothermal collapse, followed by a warm-up from 10 to 200 K. Warm-up timescales are chosen to approximate low-, intermediate-, and high-mass star formation. We also adjust initial solid-state abundances to explore the influence of ice composition on observable hot-core species. With such a large number of new species and reactions, here we set up the basic network using plausible values for chemical quantities and physical parameters, leaving the full parameter space to be explored in future papers.

The chemical and physical model is presented in Section 2, and the results and discussion in Section 3. The influence of granular ice-mantle composition is explored in Section 4. Conclusions are presented in Section 5. The Appendix gives detailed chemical information regarding the formation and destruction mechanisms of all the new complex species included in the model.

2. Model

2.1. Chemical Network

We have used as the basis for our extended chemistry the latest version of the Ohio State University gas-grain network (Garrod et al. 2007), which is based on the *osu.2005* gas-phase network. To this set we have added 50 new neutral species, and a further 32 ionic species, along with a large number of associated chemical reactions. In general, for every new grain surface-formed species included, the following new reactions and mechanisms are added to the network: accretion; thermal evaporation; grain-surface chemical reactions;

gas-phase and grain-surface photodissociation, *via* both the cosmic ray-induced UV field ($\zeta = 1.3 \times 10^{-17} \text{ s}^{-1}$) and the external interstellar radiation field (ISRF); and gas-phase ion–molecule reactions. In most cases, ion–molecule reactions involving new complex molecules result in a protonated complex ion. Dissociative recombination routes were added for those ions not already present in the network. A sticking coefficient of $S = 0.5$ is assumed for all neutral species. The reactive desorption mechanism of Garrod et al. (2007) is not included here; test runs show that its effects are generally small in this case. Evaporation due to cosmic ray-induced grain heating is included, but is generally weak, due to the ice-surface binding-energy values used here. The complete reaction network includes approximately 7500 reactions, and is available online at <http://www.physics.ohio-state.edu/~eric/research.html>.

2.1.1. *New grain-surface chemistry*

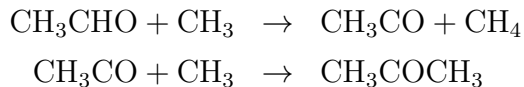
We begin with the assumption that complex organic molecules may be formed on grain surfaces from large radicals primarily derived from the icy mantles. We consider reactions between the radicals H, OH, CO, HCO, CH₃O, CH₂OH, CH₃, NH and NH₂, all of which (except H and CO) are mainly derived from the photolysis of the major ice-mantle constituents H₂O, CH₄, H₂CO, CH₃OH, or NH₃. We use the term ‘radical’ loosely, either to mean an atom/molecule that has at least one unpaired electron, and which will therefore readily react; or an unsaturated molecule, primarily CO – whose multiple bonds may be broken according to some activation energy. Dependent on their state of hydrogenation, the radicals listed above may react together either to form other radicals, or stable (typically saturated) molecules. We designate as ‘primary radicals’ those radicals (as listed above) that derive directly from photodissociation of ices or from accretion from the gas phase. We designate as ‘secondary radicals’ those species with unpaired electrons that form by reactions between primary radicals. The primary and secondary radicals may further react to produce stable (typically saturated) species. In some cases, the reactions have activation energies; those without barriers make up a subset of the reactions suggested by Allen & Robinson (1977). We assume that reaction occurs only at the radical sites and that no intramolecular rearrangement occurs upon reaction; hence the structure of the component radicals is retained in the product. Many structural isomers may thus be formed through the combination of primary and secondary radicals.

Figures 1 & 2 show all reactions between primary radicals, and between primary radicals and secondary radicals, a few of which were already present in the network. The reaction $\text{CO} + \text{HCO} \rightarrow \text{COCHO}$ is excluded due to its endothermicity (based on the formation enthalpy of the COCHO radical as determined by Ponomarev & Takhistov 2005). Primary-radical

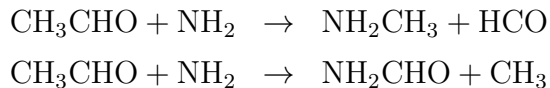
reactions with CO are assumed to have activation energies; the reactions $\text{H} + \text{CO} \rightarrow \text{HCO}$ and $\text{OH} + \text{CO} \rightarrow \text{CO}_2 + \text{H}$ ($E_A = 2500 \text{ K}$, 80 K , respectively) are treated as in previous models (Woon 2002; Ruffle & Herbst 2000, 2001b). The $\text{CO} + \text{CO}$ reaction is assumed to have a significantly higher barrier and is thus omitted. Newly-added CO reactions are assigned an activation energy of 1500 K , based on values in the NIST Chemical Kinetics Database (<http://kinetics.nist.gov/kinetics/index.jsp>). Some primary–secondary reactions involving NH-bearing species can result in unsaturated products; see Figure 2. For simplicity, we allow these products to subsequently react only with hydrogen (not shown).

Diffusion energy barriers, E_b , for each radical are also noted in Figures 1 & 2 to indicate the order in which different radicals become mobile on the grain surface during the warm-up phase; see Section 2.1.2. The mobility of the reacting species with the lower E_b value dominates the reaction rate; however, the availability of the reactants is also important, and varies in a more complex manner, according to both the gas-phase and grain-surface chemistry.

Besides the basic radical–radical addition reactions, we allow reactions between primary radicals and species that contain an aldehyde functional group ($-\text{CHO}$), in cases where such reactions are expected to be exothermic. Affected species include actual aldehydes like formaldehyde and acetaldehyde (CH_3CHO), but also formic acid (HCOOH), formamide (NH_2CHO), and the ester, methyl formate (HCOOCH_3). Figure 3 shows all of these reactions, with their activation energies in K. These types of reactions have not been considered in previous grain-surface models. *Ab initio* studies show that the barriers to radical abstraction of an aldehyde proton are much lower than the barriers to radical addition to the aldehyde group (Hippler & Visckolcz 2002). Some complex organics observed in hot cores may be formed from aldehyde group-bearing radicals produced in this way, followed by further primary–secondary radical combination reactions, e.g.



In some cases, instead of the abstraction of a hydrogen atom from the aldehyde group, the substitution of the attacking radical for a functional group on the saturated molecule may be possible, e.g.



Substitution reactions are assigned activation energies $E_A = 2400 \text{ K}$. Abstraction reactions are assigned $E_A = 2850 \text{ K}$, with the exception of OH reactions, for which we assume $E_A =$

1500 K. Estimates are based on similar reactions listed in the NIST online Chemical Kinetics Database (<http://kinetics.nist.gov/kinetics/index.jsp>), but measured values are used where available. Estimates are in agreement with values determined in the *ab initio* studies of Hippler & Visckolcz (2002). The addition of hydrogen to formaldehyde, as to CO, has a barrier of 2500 K. The two possible products, CH₃O and CH₂OH, form at equal rates.

It should be noted that those species already present in previous gas-grain networks may be involved in other reactions not listed in Figures 1 – 3; we illustrate only those reactions that involve exclusively the nine primary radicals we identify above and their secondary-radical products.

2.1.2. Surface-reaction rates and barriers

Grain-surface reaction rates are treated in the same way as in GH06. Surface-based species are assigned binding (desorption) energies, E_D , and diffusion barrier energies, E_b . Reactions occur *via* the Langmuir-Hinshelwood mechanism, i.e. reactants migrate around the grain surface until they meet at a binding site. Migration occurs by thermal hopping of reactants over the barrier E_b between sites; quantum-tunnelling effects are assumed to be insignificant (Katz et al. 1999). Hence, the diffusion energy barriers define the rates at which reactions take place. Activation-energy barriers to reaction, E_A , may be overcome thermally (which introduces a simple Boltzmann factor to the reaction rate), or *via* quantum tunneling, whichever is faster. Therefore, where E_A/T is ‘large’, the activation barrier term loses its temperature dependence. We refer the reader to Hasegawa & Herbst (1992) for a full explanation of grain-surface reaction rates.

In this study, the modified rate treatment sometimes used for hydrogen reaction rates (Caselli et al. 1998; Shalabiea et al. 1998) is discarded. This treatment was employed to remedy inaccuracies when hydrogen abundances fall to less than one atom per grain. While the method has had moderate success in the low-temperature conditions of dark clouds where hydrogen chemistry is dominant, its extension to the wide range of temperatures used in this model is anomalous when so many active surface radicals are considered. Without a clear and well-tested method of extending the treatment to such a regime, we cannot justify its inclusion. However, the inclusion of the modified rates for hydrogen atoms alone has no significant effect on the results of this model.

The grain surface is defined through E_D and E_b , where $E_b(i) = \frac{1}{2}E_D(i)$ for all species i . Values are representative of an amorphous water ice surface. As in GH06, we interpolate experimental binding energy values for certain key species (Collings et al. 2004) by simple

addition or subtraction, to produce values for all other species in our set. Therefore, to the measured CO value, we add the H value to get HCO, and again to get H₂CO. Attention is paid to species that possess an -OH functional group, as hydrogen bonding to the water-ice surface may significantly increase their binding energies (Collings et al. 2004). Hence, the structurally isomeric radicals CH₃O and CH₂OH are treated differently:

$$E_D(\text{CH}_3\text{O}) = E_D(\text{CO}) + 3 \times E_D(\text{H})$$

$$E_D(\text{CH}_2\text{OH}) = E_D(\text{CH}_3\text{OH}) - E_D(\text{H})$$

The measured value for methanol is elevated due to hydrogen bonding to the ice surface. Hence CH₂OH is much more strongly bound than CH₃O, and so it requires greater dust temperatures to become mobile, or evaporate. This distinction is critical, as the two species are chemically different since their radical sites are on different atoms. Through a similar construction of binding energies, the distinction propagates through to their products. Thus, we may investigate, for example, the difference between the formation of structural isomers methyl formate (HCOOCH₃) and glycolaldehyde [CH₂(OH)CHO], and the difference in their own behavior due to their different binding energies.

The evaporation of water, the primary constituent of icy grain mantles, should result in the co-desorption of any other species remaining in the ices (Collings et al. 2004). In order to take account of this structural aspect of mantle evaporation, we allow E_D values to be no greater than that of H₂O. Diffusion barriers are unaffected by this adjustment.

2.1.3. *New grain-surface and gas-phase photodissociation routes*

Excluding atomic hydrogen, which is mostly accreted from the gas phase, the grain-surface primary radicals derive from the icy grain mantles formed during the cold collapse phase; either directly (CO), or through cosmic ray (CR) -induced photodissociation of molecular ices. In addition, HCO and CH₃O/CH₂OH may be formed *via* the hydrogenation of CO and H₂CO, respectively.

Gredel et al. (1989) calculated rates for the CR-induced photodissociation of a number of astrochemically important species, including those concerned here. However, the products remain uncertain. We retain the treatment of Gredel et al. for H₂O, CH₄ and NH₃ to give H, OH, CH₃, NH, and NH₂. For H₂CO we include an additional channel, producing HCO + H; see Table 1.

The CR-induced photodissociation of CH₃OH is especially important to this model. Gredel et al. suggest two photodissociation branches, CH₃ + OH and H₂CO + H₂. However, several potential channels have been shown through both theory and experiment to

be important in methanol dissociation mechanisms, including those producing the radicals CH_2OH and CH_3O (see Chang & Lin 2002, 2004, and references therein). The adoption of the Gredel et al. channels is convenient for purely gas-phase models, which do not typically include $\text{CH}_3\text{O}/\text{CH}_2\text{OH}$ radicals. However, our model includes both radicals, because of their importance to complex surface chemistry. Given that the intramolecular rearrangement involved in the $\text{H}_2\text{CO} + \text{H}_2$ channel of methanol dissociation is rather unlikely in an ice matrix, we have replaced this channel with $\text{CH}_3\text{O} + \text{H}$ and $\text{CH}_2\text{OH} + \text{H}$. The chosen rates are slightly lower than those for the $\text{CH}_3 + \text{OH}$ channel, in agreement with the H-atom ejection channels of other molecules. The two structural isomers are assumed to be formed at the same rate. These branching ratios may strongly influence structural isomerism in the surface-formed complex molecules; we will investigate these effects in depth in a future study.

All of the new complex species added to this network are assigned CR-induced photodissociation channels. In the absence of experimental data for many of these species, assumptions must be made about the products and rates. Molecules are assumed to dissociate primarily into their constituent functional groups, which is facilitated by our explicit treatment of a large number of radical species. We avoid channels that result in a great degree of structural rearrangement, which would be unlikely in an interstellar environment. Where not otherwise available, representative rates are selected from the existing ratefile, according to the pair of atoms or groups whose bond is broken. This is a simplistic approximation that ignores the specific mechanics of photodissociation in a particular molecule, which are necessarily dependent on its UV absorption spectrum, the spectrum of the CR-induced radiation field, the partition of energy within the molecule, and its specific quantum state. However, this method does take indirect account of the energy required to break the bonds, and allows for the most accurate estimation of dissociation rates possible given the incomplete laboratory information available.

All photodissociation channels are applied to gas-phase and grain-surface species with the same rates and products, as in previous models. The accuracy of this approach is difficult to ascertain, as there is currently very little data on relative rates in the gas phase and on grain surfaces. Kroes & Andersson (2006), and references therein, show that the first absorption band of crystalline water ice is centered at an energy $\sim 15\%$ higher than the gas-phase band, indicating that the dissociation rates may be different for this molecule.

Photodissociation caused by the ISRF is also considered, using the same approach. However, this mechanism is relatively unimportant, as visual extinctions are typically high, except during the earliest stages of the isothermal collapse phase, at which time the abundances of complex molecules are negligible.

2.1.4. *New gas-phase ion–molecule reactions, dissociative recombination*

Gas-phase destruction routes involving the dominant ions He^+ , C^+ , H_3^+ , HCO^+ , and H_3O^+ have been added for each of the new species introduced through grain-surface chemistry. Reactions of new species with C^+ ions is assumed typically to result in charge transfer, leaving complex molecular structure intact, whilst reaction with He^+ results in fragmentation. Reaction with molecular ions leads in most cases to protonation. The complex ionic species which result from the new reactions have been added to the network, where not otherwise present.

Rate coefficients are calculated using experimental (or otherwise, computed) dipole moments or polarizability data, available from the NIST Computational Chemistry Comparison and Benchmark Database (NIST 2005). In the case of linear, non-polar molecules, simple Langevin rates are used, while the method of Herbst & Leung (1986) is adopted for all other molecules. Where no calculated or experimental values are available, dipole moments are estimated by comparison to structurally similar molecules. Since the Herbst & Leung method produces a linear dependence on dipole moment, we should expect the calculated rates to be as accurate as our estimate of this quantity. Measured dipole moments for complex molecules are typically in the range of 1 – 5 debye, so ion–molecule reaction rates are unlikely to be inaccurate by more than a factor of a few.

The introduction of new ionic species requires new dissociative recombination reactions to be introduced. The branching ratios of such reactions have recently come under particular scrutiny. Geppert et al. (2006) have shown that the $\text{CH}_3\text{OH} + \text{H}$ channel accounts for less than 5% of protonated methanol recombinations; the strongest channels represent three-body break-ups. For protonated complex molecules, we assume that two-fragment channels represent 5% each, and that the remainder is evenly split between channels with three (or more, where applicable) fragments. In analogy with the new photodissociation reactions, we allow fragmentation primarily between functional groups within the molecule (including the molecule–proton bond). Other channels are allowed if they result in stable (and especially, saturated) products, with minimal structural re-arrangement of the molecule. Total rate coefficients of $k = 3 \times 10^{-7} \text{ cm}^3 \text{ s}^{-1}$ are assigned, in keeping with other large-molecule values.

2.2. **Physical model and initial conditions**

We adopt the same two-phase physical model as GH06. In the collapse phase, the nascent hot core undergoes isothermal collapse at 10 K, from a density of 3×10^3 to 10^7

cm^{-3} . The collapse phase begins at a visual extinction of 1 magnitude, growing to over 200. We include the H_2 and CO self-shielding functions of Lee et al. (1996), to ensure a more reliable treatment of hydrogen and CO in the initially diffuse physical conditions of the collapse phase. For the purposes of self-shielding, we designate an H_2 abundance of 1/3 and a CO abundance of 10^{-5} to the outer envelope, and assume a total hydrogen column of $1.6 \times 10^{21} \text{ cm}^{-2}$. As the central visual extinction grows throughout the collapse, we allow the H_2 and CO column densities to increase according to

$$N(i) = N_{\text{init}}(i) + X(i) \times (1.6 \times 10^{21}) \times (A_V - 1)$$

where $X(i)$ is the fractional abundance with respect to total hydrogen as computed in the code. Initial abundances are the so-called low-metal abundances of Graedel et al. (1982) except for species He, C^+ , N, and O, whose values are selected from the most recent diffuse cloud values (Wakelam & Herbst, unpublished), see Table 2. The behavior of sulfur and the other heavy elements included in the model on grain surfaces is not well understood. Indeed, the form and location of sulfur in dense regions is an unanswered question in astrochemistry; we do not attempt to answer it in this paper, and we adopt the canonical (low) dense cloud abundances for atoms heavier than oxygen.

In the warm-up phase, the collapse is halted, and the temperature grows from 10 to 200 K, over three timescales: 5×10^4 , 2×10^5 and 1×10^6 years, corresponding to models F (fast), M (medium), and S (slow), respectively; see Table 3. Following Viti et al. (2004), GH06 identified these timescales with high-, intermediate- and low-mass star formation, respectively. However, Aikawa et al. (2007) argue that the warm-up timescale is dependent on the ratio of the size of the warm region to the infall speed, rather than on the overall speed of star formation. This would suggest the contrary relation between mass and warm-up timescale. This point is discussed in relation to chemical abundances in later Sections. We concentrate on the T_2 temperature profile adopted by Garrod & Herbst (2006), where $T(t) = 10 + k \cdot t^2$, measured in Kelvin, at time t . Gas and dust temperatures are assumed to be well coupled, due to the high densities and visual extinctions, so we assume $T_K = T_{\text{grain}}$ at all times.

While we use a single-point model, the resulting time-dependent data may also be interpreted as representing a range of distances from the hot-core center, with the innermost parts being the most evolved and achieving the highest temperatures. As such, we may understand the chemistry of the colder, more extended regions of a hot core using this single model.

3. Results and Discussion

The results of models F, M, and S are presented, corresponding to different warm-up timescales. Discussion of the chemistry is restricted here to general trends, while specific, key aspects are discussed further in following Sections. A more detailed discussion of the chemical behavior of individual species or classes of species is given in the Appendix.

Figures 4 – 6 show abundances with respect to time and temperature for models F (fast warm-up), M (medium), and S (slow), all of which undergo the same collapse-phase evolution. Each Figure panel shows a subset of the molecular species included in the model, beginning with simple ice-constituents (panel a). Solid lines indicate gas-phase abundances; dotted lines of the same shade/color indicate the grain-surface abundance of that species. Included in these plots are many of the most commonly observed species, as well as a suite of unobserved complex organics predicted to form *via* the new grain-surface chemical network.

Table 3 shows the peak gas-phase abundances of species plotted in Figures 4 – 6, for each evolution timescale, as well as the temperatures at which those peak values are achieved.

The results demonstrate that the consideration of a surface chemistry involving a small set of radicals derived from dominant grain-surface ice components produces a wealth of information on complex organic molecules – many of which have not yet been detected in interstellar space. The grain-surface production of species investigated by GH06 is maintained and their structural isomers are also formed, along with yet more structurally-complex molecules.

The composition of the ice is crucial to the chemistry both on grains and in the gas phase, as methanol and formaldehyde provide most of the basic radicals that produce organic species. The grain-surface abundances of these species also directly determine their peak gas-phase abundances upon evaporation; surface chemistry is not capable of strongly diminishing their surface abundances. These species’ major destruction route on the grains is photodissociation by the CR-induced UV field, producing reactive radicals.

The injection of H_2CO into the gas phase strongly influences the chemistry at intermediate temperatures. It provides the material for the formation of other species, but also acts as the dominant reaction partner for gas-phase ions, facilitating the survival of the other newly-formed species in the gas phase for significant periods. For model F, this includes complex molecules like methyl formate and dimethyl ether.

In general, those species formed on grains during the warm-up phase benefit from longer evolution timescales, as more time is spent at their optimal temperatures of formation. Later, following the main period of formation, abundances of surface species are somewhat

attenuated by CR-induced photodissociation, especially over the long timescale of model S. Additionally, the longer periods at high temperature seen in models M and S allow hydrogen-abstraction reactions to destroy grain-surface aldehyde group-bearing species.

Long warm-up timescales also limit the long-term survival of molecules that evaporate in advance of the remainder of the ices. When the major ice constituents H_2O , NH_3 and CH_3OH evaporate, they become the dominant reaction partners for gas-phase ions (similar to H_2CO at earlier times), damping ionic abundances and thus limiting the destruction of other species. Complex molecules that spend long periods in the gas phase before this may be strongly diminished.

3.1. Structural isomers

HCOOCH_3 , $\text{CH}_2(\text{OH})\text{CHO}$ and CH_3COOH are structural isomers that have been detected in several star-forming regions (see Snyder et al. 2002, and references therein). However, their relative abundances are puzzling, particularly in light of the failure of gas-phase chemistry to account for methyl formate (Horn et al. 2004). Their relative abundances in the hot core Sgr B2(N-LMH) are, respectively, 52:1:2 (Snyder et al. 2002). It is arguable that if all three were formed by similar processes on grain surfaces, for example by single-atom addition reactions, then their observed abundances should be similar, assuming comparable destruction mechanisms.

In fact, the structural differences in these species can be explained by different combinations of the primary radicals considered here. In this model, methyl formate and glycolaldehyde have similar formation routes based on addition of HCO to CH_3O or CH_2OH , whose production rates are the same. Hence, the resultant molecules are similarly abundant. However, the lower abundance of acetic acid relative to methyl formate is reproduced in our model, especially with shorter warm-up timescales, because it has a very different formation route. The secondary radical CH_3CO combines with OH , but the CH_3CO is derived not from direct addition of CH_3 and CO , but from photodissociation of acetamide, or hydrogen abstraction from acetaldehyde, both of which are formed earlier. These routes would suggest a correlation between the abundance of acetamide and/or acetaldehyde, and that of acetic acid. The relative abundances of methyl formate and glycolaldehyde may be influenced by disparities in the $\text{CH}_3\text{O}/\text{CH}_2\text{OH}$ branching ratios resulting from methanol photolysis and/or formaldehyde hydrogenation. However, it is clear that this type of grain-surface chemistry can address the observed relative abundances of structural isomers.

This model also permits the study of the structural isomers dimethyl ether and ethanol.

They are formed by addition of the CH_3 radical to either CH_3O or CH_2OH , which primarily occurs when CH_3 becomes mobile, around 30 – 40 K. As above, the equal branching of $\text{CH}_3\text{O}/\text{CH}_2\text{OH}$ production routes results in grain-surface formation of these species in very similar quantities. However, dimethyl ether desorbs strongly around 70 K, while the -OH group of $\text{C}_2\text{H}_5\text{OH}$ ensures that ethanol co-desorbs with water at high temperatures. While longer warm-up timescales can result in very large quantities of dimethyl ether forming on grains, its early evaporation results in fast gas-phase destruction (see Section 3, above). This means that gas-phase production of this species (following methanol evaporation) is always dominant over grain-surface formation, a result in accordance with the analysis of Peeters et al. (2006). Therefore, dimethyl ether should not be a good indicator of grain-surface chemistry *per se*. The substantial quantities of ethanol observed in star-forming regions may be assumed to be such an indicator, and indeed suggests that CH_3O is well-supplied on grain surfaces. Calculated abundances for dimethyl ether and ethanol are correspond with typical observed values.

3.2. Rotational temperatures

One of the most striking results of this work is that the peak temperatures of many hot-core molecules (Table 3) show agreement with observed rotational temperatures. In particular, the low-temperature molecules identified by Bisschop et al. (2007), CH_2CO , CH_3CHO , and H_2CO , display excellent agreement. In the model, these species evaporate from the grains at low temperatures, as determined by their binding energies to water ice. For long warm-up timescales, high gas-phase abundances are sharply defined in a narrow, low-temperature range. For short warm-up timescales, high abundances are maintained to high temperatures.

Bisschop et al. (2007) also identify HCOOH as a ‘cold’ molecule, and, ignoring the late-time peak caused by grain-surface evaporation, HCOOH does indeed peak at low temperatures in our model. This peak is caused directly by reaction of evaporated formaldehyde with OH molecules in the gas phase to form formic acid. Nummelin et al. (2000) observe a low rotational temperature for HCOOH in Sgr B2(N), at $T_{rot}=74$ K, albeit with sizeable error margins. Such evidence may indicate that HCOOH is strongly *destroyed* on grains at late times, before evaporation takes place. It would not be sufficient to suggest that it is merely *not formed* on grains, as much of the formic acid present on grains at late times has its origin in the accretion of the gas-phase species formed from formaldehyde at ~ 40 K. This may indeed suggest that hydrogen abstraction processes acting on aldehyde group-bearing species are yet stronger than we assume here.

The model shows strong CH_3CHO evaporation at low temperatures, which is qualita-

tively in agreement with observed rotational temperatures (Nummelin et al. 2000; Bisschop et al. 2007), although these are not well-defined. Our model also suggests a high-temperature peak for long warm-up timescales, due to formation from evaporated hydrocarbons, whose abundances grow slowly on grains. High-temperature acetaldehyde detections may therefore signify long lifetimes in hot-core sources.

CH₃CN, like HCOOH, achieves an early- and a late-time peak, although the latter, due to evaporation of CH₃CN, is much stronger. The former peak is produced indirectly by the evaporation of HCN from grains. Bisschop et al. (2007) identify CH₃CN solely as a ‘hot’ species, but Nummelin et al. (2000) obtain a low rotation temperature of 46 K in their Sgr B2 NW position, which was chosen for its lack of star-forming activity.

H₂CO is also desorbed at low temperatures in this model, and is important in the formation and survival of other species. Bisschop et al. (2007) find H₂CO rotational temperatures from $\sim 70 - 90$ K, and van der Tak (2000) find temperatures in this range toward a number of massive YSOs. This does not necessarily contradict our somewhat lower formaldehyde evaporation temperature, as H₂CO abundance remains high up to temperatures of 80 K and 200 K in the medium (M) and fast (F) models, respectively. In addition, two of van der Tak’s sources yield temperatures close to 200 K. A more intricate treatment of the icy grain mantles in the model might yield a high temperature peak in formaldehyde separate from its evaporation at ~ 40 K, as we do not explicitly deal with trapping of weakly-bound species in the amorphous ice matrix (Collings et al. 2004). Species formed early during the collapse phase may be trapped until the entire mantle is evaporated. This could also be the case with, for example, CO, CO₂, CH₄, and perhaps HCOOH. Indeed, the somewhat elevated excitation temperatures of gas-phase CH₄ towards some protostellar sources, reported by Boogert et al. (2004) and references therein, could indicate trapping of methane in the deeper water-ice layers. Explicit modeling of the individual ice layers would shed some light on these issues. As in GH06, most H₂CO in the current model is formed late in the collapse phase, and would therefore exist in the outermost ice layers.

Unlike the results for many other species, this model does not reproduce the low rotational temperatures for glycolaldehyde observed by Hollis et al. (2000, 2001, 2004) in Sgr B2(N). They suggest a warmer (~ 50 K) glycolaldehyde component surrounded by a cold (~ 8 K) one. In our model, glycolaldehyde is formed on the grains at around 30 – 40 K; however, it is not desorbed strongly until temperatures of ~ 110 K are reached. Excluding a gas-phase formation mechanism for glycolaldehyde, two possible scenarios exist for its presence in cold gas. The first scenario, as suggested by Hollis et al., is that Sgr B2(N) has undergone shocks, in which case the temperature progression of the grains is disrupted, after a period with $T_d > 30 - 40$ K at which glycolaldehyde may form. The second scenario

involves a non-thermal desorption process, regardless of the heating mechanism (ie. protostellar switch-on, or shocks). Such may be the one suggested by Garrod et al. (2006, 2007) for the formation of gas-phase methanol in cold clouds, whereby the energy of formation of a surface molecule may break the surface–molecule bond with a probability on the order of 1%. This would result in glycolaldehyde being desorbed most strongly as it forms on the grains, at temperatures close to the observed 50 K. It could inject no more than $\sim 1\%$ of the total amount formed on grains, however; approximately $10^{-10}n_H$ in this model.

The inclusion of hydrogen-abstraction reactions for aldehydes shows that they may be destroyed on the grains at high temperatures given sufficient time. These mechanisms could explain the apparently large spatial scale of glycolaldehyde in the context of shock-induced desorption. In more extended regions, shocks could desorb glycolaldehyde from grains before they have time to be processed at high temperatures, while hot-core regions which gradually achieve high temperatures could be depleted of their glycolaldehyde before evaporation becomes efficient. Hence, glycolaldehyde would be a tracer of sudden desorption or temperature increase.

3.3. Complex chemistry in low-mass star-forming regions

The low-mass protostellar analogs of hot cores, the so-called ‘hot corinos’, also show strong signatures of complex molecules (Cazaux et al. 2003; Bottinelli et al. 2004a,b). Observationally, there appear to be differences between the low-mass and high-mass scenarios. Bottinelli et al. (2007) report that the ratios of HCOOCH_3 , CH_3OCH_3 and HCOOH to their putative parent molecules, CH_3OH and H_2CO , appear greater for hot corinos than hot cores, with the HCOOH ratios being more strongly affected. These observations may be explained in terms of our model: shorter periods (i.e. model F) between the evaporation of HCOOCH_3 and CH_3OCH_3 at $\sim 70 - 80$ K and the evaporation of water and other ice components at ~ 110 K improves the survival of these more complex species (see Section 3). Also, grain-surface destruction of complex species, especially HCOOH and other aldehyde group-bearing species, is stronger in models with longer warm-up timescales. This may suggest that the observational differences are due to the faster transit of the gas through temperatures of $\sim 50 - 100$ K in the hot-corino case. However, the short-timescale model (F) produces lower abundances of complex molecules, due to the shorter periods at $\sim 10 - 50$ K at which many complex molecules are efficiently formed. This indicates that much longer periods in this temperature range than we assume may be appropriate for hot corinos. The recent chemical/hydrodynamic model of prestellar to low-mass protostellar evolution by Aikawa et al. (2007) does indeed indicate longer times at low temperatures than assumed here, and much

shorter times at high temperatures.

The implications for methyl formate and dimethyl ether are predicated on their having significantly lower binding energies than H_2O . An interesting test of these results would be whether the ratios with H_2CO and CH_3OH hold for species with much greater binding energies.

Shorter high-temperature timescales would also tend to reduce abundances of the more exotic species formed on grains *via* the addition of two tightly-bound radicals at high temperature. Examples of this type of molecule include urea, $(\text{NH}_2)_2\text{CO}$, and ethylene glycol, $(\text{CH}_2\text{OH})_2$. The model indicates that the very complex species of this sort may be much less prevalent in low-mass star-forming regions.

3.4. Large complex molecules

This model predicts a number of large complex molecules to be formed with significant abundances; see Figures 4 – 6, panels e – j. Many of these species have not been detected in the interstellar medium. We are aware through personal communication that directed observational searches are ongoing for some of these more complex species. However, laboratory spectra for many of these molecules do not exist. We hope that this model will provide impetus for such spectra to be obtained.

The newly-predicted molecules that are most abundant and robust to changes in evolution timescale – and therefore the best candidates for observational investigation – are the OH-bearing species CH_3OOH , $\text{CH}_2(\text{OH})_2$ and HOCOOH ; the amide-group species NH_2COOH and $(\text{NH}_2)_2\text{CO}$; and the amine-group species CH_3ONH_2 , $\text{CH}_2(\text{OH})\text{NH}_2$, and NH_2OH . Each of these species and the many other complex species predicted to form by this model are discussed in detail in the Appendix.

The most abundant complex molecules seem to be those that are derived from the reaction of primary radicals alone, and not secondaries. Secondary radicals form at the same time as primaries (at intermediate temperatures), but their reactive nature and relative immobility at these temperatures mean they are most likely to be hydrogenated to their fully-saturated forms. The secondary radicals typically become mobile much later, at a time when they are no longer being directly formed from primary-primary addition, but rather by CR-induced photodissociation of larger species, or by hydrogen abstraction in the case of species bearing the -CHO functional group. Longer timescales allow more time to produce secondaries at appropriate temperatures for them to be independently mobile.

4. Ice composition

The results discussed above are produced by a two-stage model of cold collapse and warm-up. However, the initial conditions of the collapse phase, and the physical parameters themselves, are not well constrained. In particular, it appears that the (cold) dust temperature is important to the ultimate composition of the icy grain mantles (Ruffle & Herbst 2001b); variations of a few Kelvin can strongly affect the efficiency of hydrogenation, which is the dominant mechanism.

Table 5 shows observationally determined ice compositions towards two embedded YSOs, and towards the galactic center infrared source, Sgr A* (Gibb et al. 2000). Also shown are model values for the end of the collapse phase. The observed ice abundances appear mostly similar in composition to those achieved with this model, however it is unclear precisely how much processing these ices have already undergone, or indeed whether they are a fair representation of the state of the ice mantles near the centers of hot cores.

In comparison to observed values, methane seems to be overproduced in our model, whilst surface CO₂ is significantly underproduced. The latter is a long-standing problem in gas-grain modeling (Ruffle & Herbst 2001b). Higher initial temperatures may improve agreement in both of these cases. The lack of grain-surface formic acid in our models may be due to the lack of CO₂, which could presumably be hydrogenated to HCOOH. Alternatively, it may be related to grain processing associated with heating and the onset of star formation.

The gas-phase methanol abundance seen in our models during the warm-up phase may be somewhat high at $\sim 10^{-5}n_H$; however, as it is almost entirely derived from grain-surface evaporation, this implies that it is overproduced on grains during the cold collapse phase. A similar grain-surface overabundance may also be true for formaldehyde.

Since these two molecules, along with methane, are important sources of radicals on the grains, we have run further warm-up models with grain-surface abundances of these species reduced by a factor of 10; see Table 5. We have investigated reductions in each of these species individually, but they may easily be examined together. We do not include changes in the CO₂ abundance in this discussion, as it is not a major source of radicals. Figures 7 – 9 show time-dependent abundances for each of the three models: F(ice), M(ice) and S(ice), corresponding to fast, medium and slow warm-up, respectively (Table 3).

The effect of CH₄ reduction is in fact small, if considered in isolation. This is due to the possibility of CH₃ production from photodissociated methanol. In fact, methanol is the dominant producer in the 30 – 40 K temperature range. The reduction of methanol is required for a strong effect on CH₃-related species, e.g. CH₃NH₂.

The impact of reduction in H_2CO on grains is strongest for the shorter timescales; longer periods at low temperature allow the hydrogenation of CO to H_2CO , such that for model S the H_2CO abundance is little altered. However, a factor of a few lower grain-surface abundance has a strong effect on its survival in the gas phase. Formaldehyde is the most important reaction partner for ions at intermediate temperatures, damping abundances of destructive ions, so the long-term survival of many other species in the gas phase is also diminished. This strongly affects methyl formate, whose release from the grains no longer coincides with large gas-phase formaldehyde abundances, even in model F(ice).

Lower formaldehyde abundance also lessens the abundance of HCO. However, this radical may also be formed by hydrogenation of CO. For short warm-up timescales, the reduction in both CH_3 and HCO radicals (formed from H_2CO) greatly reduces acetaldehyde abundances.

The reduction in methanol abundance has a strong effect on complex-molecule abundances both in the gas phase and on grain surfaces, but its effects are largely predictable. Species formed from the radicals $\text{CH}_3\text{O}/\text{CH}_2\text{OH}$ suffer reductions of around 10 times, or more if they are formed also from CH_3 or HCO. This clearly creates additional problems for methyl formate, as, even for model S(ice), it is only formed on grains to an abundance of a few $\times 10^{-9}n_H$. The effects are yet stronger for those species which are doubly dependent on methanol-derived radicals, like ethylene glycol, and gas phase-produced dimethyl ether.

Clearly these reductions greatly influence the complex chemistry in the model, and the most important of the three ice-abundance reductions is that of methanol. These reductions also place abundances of some of the more exotic species produced in this model firmly beneath the level of detectability, especially for shorter warm-up timescales.

The failure to produce sufficient quantities of methyl formate in particular, and, to some degree, dimethyl ether, may suggest either that methanol CR-induced photodissociation is faster than assumed in our model, or that the hydrogenation of H_2CO to $\text{CH}_3\text{O}/\text{CH}_2\text{OH}$, which has an activation energy barrier, takes place more efficiently to make up for a lower contribution from methanol. Other possibilities include some alternate route for the reduction of methanol, perhaps a barrier-mediated hydrogen-abstraction mechanism similar to those assumed for aldehydes, albeit with a greater activation energy. In previous models it has been assumed that the hydrogen abstraction reaction $\text{OH} + \text{H}_2\text{CO} \rightarrow \text{HCO} + \text{H}_2\text{O}$ has no activation energy barrier, whereas we assume a value of 2500 K. GH06 found this to be the most important HCO-production mechanism, and so the higher value (used in this model for consistency with other similar reactions) may have a large influence on complex-molecule formation.

Recent *Spitzer* surveys of low-mass YSOs (Boogert et al. 2008) now indicate that methanol may indeed be as abundant as our ‘standard’ ice values in some sources, at 1 – 30 % with respect to H₂O, whilst ammonia may be somewhat less abundant than we assume, at 1 – 5 %. The influence of these new data on the chemical models should be explored in future work.

4.1. Comparison with observations

The galactic-center hot-core source Sgr B2(N) is well-known for its rich chemistry, and some of the more complex species we model here have only been detected along that line of sight, making it an apt subject for comparison with the model. It is almost certainly not the case that the dynamics or morphology of Sgr B2(N) are as simple as assumed in the model; however, it is generally accepted that at least one hot-core source resides in the very central region, regardless of shock dynamics in more extended regions. Here we compare abundances and rotational temperatures observed toward Sgr B2(N) with values from our reduced ice-abundance models. This provides gas-phase and grain-surface methanol and methane abundances more in keeping with observations, as well more acceptable gas-phase formaldehyde values.

Table 6 shows calculated peak abundances for a range of molecules, along with the gas/dust temperature at that peak, for each of the warm-up timescales of the reduced ice-composition run. For some species, both early and late peaks are shown, especially where there is observational evidence of more than one rotational temperature component. Beside the modeled values we list observed abundances, calculated from beam-averaged column densities assuming $X(\text{H}_2)=0.5$ and $N(\text{H}_2)=3 \times 10^{24} \text{ cm}^{-2}$ (Nummelin et al. 2000). Also shown are the associated rotational temperatures, and the FWHM beam size. The majority of these observational values are derived from the survey by Nummelin et al. (2000). Where only abundances of isotopomers are available, we assume isotopic ratios of: $\text{C}^{12}/\text{C}^{13}=70$ and $\text{O}^{16}/\text{O}^{17}=2044$ (see Redman et al. 2002, and references therein), and $\text{N}^{14}/\text{N}^{15}=100$. Where two temperature components have been detected, we list them next to the early- or late-time (cold or hot) peak model abundance, as appropriate.

In a simple analysis, if the emitting molecular species in the hot core is more compact than the projected beam of the telescope, the beam-averaged emission will indicate a molecular column density that is lower than the true value – by a factor of the squared ratio of the angular source size to the beam size. In Table 6, in cases where the model indicates that species are released from grains at high temperature, we list observational abundances adjusted for beam dilution by assuming a compact emitting source that is 5'' in size; we assume

that the $N(\text{H}_2)$ remains constant. Such cases are indicated in the *notes* column. Similarly, we compare the cold species with the unadjusted abundances for a $23''$ beam based on the assumption that these species are spatially extended, and therefore fill the beam. We set in boldface those peak-abundance temperatures that approximately agree with observational rotational temperatures. We highlight abundances that agree with observed values within approximately one order of magnitude. Such values are only highlighted in cases where the observed or re-calculated beam-sizes are appropriate to the temperatures.

Overall, the modeled abundances and temperatures match well with the observations, and succeed in reproducing values for both hot and cold components. The medium warm-up timescale, model M, appears to produce the best match. Whilst this model represents only a single point in space, we may consider the molecules that are better represented by low temperatures as being more distant from the hot-core center (and therefore more spatially extended), representing material that is less advanced in its warm-up sequence.

Discrepancies exist, and these may originate from the more subtle chemical and physical aspects of the model that are discussed above, including branching ratios, activation energies, and binding energies – especially for species such as methyl formate. Ice structure may also complicate the determination of gas-phase abundances at lower temperatures, prior to the total evaporation of grain mantles. Regarding physical conditions, shocks or radiative pumping may explain the differences between observed rotational temperatures and model peak temperatures. Other discrepancies could likely arise from uncertain observational parameters. For example, molecular partition functions often exclude vibrational contributions because only the pure rotational lines from the ground vibrational state have been measured experimentally.

Additionally, the lack of spatial-scale information for most species makes the beam-dilution correction quite uncertain. Indeed, recent CARMA observations indicate that the spatial distributions of some of the most common hot-core molecules may in fact be much more complicated than previously thought (Friedel & Snyder 2007).

5. Conclusions

Presented here is the first hot-core chemical model to employ an extensive network of grain-surface reactions for organic molecules, in addition to the standard gas-phase ion-molecule formation routes. We use a two-stage physical model incorporating the collapse and warm-up phases of a hot core to explore the chemistry in low- to high-mass star-forming regions. The photodissociation of common ice-mantle con-

stituents by the cosmic ray-induced UV field (typically removing a hydrogen atom) produces grain-surface radicals. These ‘primary radicals’ become mobile and reactive on the grain surfaces as dust temperatures increase during the warm-up phase. In this way, basic component structures may attach to one another, building up larger molecules. Further photodissociation (or hydrogen abstraction) of the resultant complex molecules provides the main source of ‘secondary radicals’, leading to an even greater degree of chemical complexity. This type of chemistry, based on a small set of radicals, can explain the formation of many complex organics that have been detected, but which previously had no plausible gas-phase formation routes. Many other complex organic molecules are also formed in this chemical network, and predictions for a number of previously uninvestigated molecules are now available.

The differing surface-binding characteristics of the grain-surface species control the order in which radicals become mobile during the warm-up phase. At temperatures around 30 – 40 K, the reaction of the mobile primary radicals HCO and CH₃ with more strongly-bound primary radicals CH₃O and CH₂OH results in the formation of methyl formate, dimethyl ether, glycolaldehyde and ethanol. These species evaporate when higher temperatures are achieved.

The production of radicals of greater complexity (secondaries) is weaker than that of primaries, due to the lower abundances of their parent complex molecules. At intermediate temperatures (~30 – 50 K), secondaries typically react with the mobile primary radicals, allowing three-carbon-atom species like acetone to form. At higher temperatures (~50 – 100 K), secondary radicals themselves may become mobile; high temperature mobility of the secondary radical CH₃CO results in reaction with OH to form acetic acid. The dependence of secondary-radical formation on the abundances of the simpler complex molecules means that primary–secondary radical additions are most effective with long warm-up timescales; hence the most complex molecules may be detectable in the most slowly-evolving sources.

Such differences between primary- and secondary-radical processes may indeed explain the disparities in observed abundances of structural isomers, most notably methyl formate/glycolaldehyde/acetic acid. While the precise relative abundances calculated for these species are not a direct match to observed values in Sgr B2(N), our network provides plausible, differing formation routes for each of the three. Agreement may be improved following further exploration of the parameter space of this model. A more extensive treatment of the ice chemistry to include esterification reactions between carboxylic acids and alcohols may also offer more insight into the differing abundances of these structural isomers.

Complex molecule formation is not restricted to grain surfaces, but may still be intricately linked to grain-surface processes. The evaporation of formaldehyde at ~40 K results in the gas-phase formation of other species, including HCOOH. Other rotationally cold species

like CH_3CHO are formed on grains and evaporate at low temperatures. Differing grain-surface characteristics may therefore be responsible for observed spatial and temperature displacements between different gas-phase molecules.

The initial ice composition was adjusted to agree with infrared observations of protostellar envelopes, reducing the amount of those ices available for primary-radical production. Comparison of this model to molecular abundances and temperatures observed in the Sgr B2(N-LMH) hot core results in a reasonable match in light of the uncertainties in the model, especially for the intermediate warm-up timescale. However, the abundances of complex molecules in the fast warm-up model are rather low in comparison to low-mass star-forming regions, with which we identify short warm-up timescales. This may indicate that the initial ice compositions in low- and high-mass star-forming regions are somewhat different; or that the low- to intermediate-temperature phases of hot-corino evolution are longer-lived than we assume in our simple model. The latter conclusion agrees with the hydrodynamic models of Aikawa et al. (2007). Nevertheless, our results support the argument that hot corinos experience shorter periods at high temperature than hot cores.

The study presented here is only the first step in probing the many chemical and physical influences on hot-core chemistry; a much larger parameter space exists than has been explored here. The branching ratios for both the photodissociation of methanol ice and the hydrogenation of formaldehyde are quite uncertain, and the activation energies for many of the grain-surface reactions are poorly defined. All of these quantities could strongly influence the degree of isomerism and molecular complexity reached in grain-surface reactions; further studies are planned.

The choice of grain-surface binding energies is particularly important for methyl formate, dimethyl ether, and acetone; the values employed here allow these species to evaporate before most other large molecules, leaving them vulnerable to gas-phase destruction. Their abundances are therefore more sensitive to warm-up timescales, and to their final grain-surface abundances, prior to evaporation. The interaction of these effects with those of branching ratios and activation energies may therefore be complex.

This model is the first such study that can explain the chemical complexity observed in both high-mass and low-mass hot cores. Much work remains, however, before a full understanding of these complicated environments can be achieved. Given the variability in abundances and temperatures amongst hot cores it is unclear whether a direct comparison between the model and observations is valid for such a small sample. We encourage systematic observational surveys that probe a range of physical and chemical conditions in star-forming regions. Given the large number of previously uninvestigated molecules predicted by this model, we also encourage additional laboratory studies to support astronomical

searches.

The chemical network employed in this model is, of course, not comprehensive. A number of unsaturated species, hydrocarbons in particular, have been detected in star-forming regions, but are not explicitly treated here, due to the complexity of the hydrogenation process, which undoubtedly involves poorly-defined activation energies. Hassel, Herbst & Garrod (submitted) have begun to address this issue. A number of cyanide species have also been detected, but are omitted from this model for the same reasons. Future models must take account of all these species, which in many cases are very abundant; however, the degree of complexity reached in this model is substantial.

RTG thanks the Alexander von Humboldt Foundation for a Research Fellowship. Support for SLWW was provided by NSF grant AST-0540459 through the UIUC Laboratory for Astronomical Imaging, and by the UIUC Critical Research Initiative program through the group of Benjamin McCall. SLWW would also like to acknowledge Geoffrey Blake for very helpful discussions regarding the chemical network as well as support during its initial development. EH acknowledges the support of the National Science Foundation for his research program in astrochemistry.

6. Appendix

Here follow detailed discussions of the results for each species or class of species represented in Figures 4 – 6. Each Section corresponds to one (or more) similarly labeled panel in the Figures. While the final abundances may change between the standard and reduced ice composition models, the overall trends discussed here are also applicable to Figures 7 – 9.

6.1. H_2O , CO , CH_4 , NH_3 , and HCO^+ (a)

The ice constituents CO and CH_4 are seen to evaporate at low temperatures (20 – 25 K), but NH_3 and H_2O remain on the grains in large quantities until a temperature of ~ 110 K is reached. The evaporation of H_2O and NH_3 ices strongly influences gas-phase ion chemistry, as is illustrated by the HCO^+ abundance. HCO^+ also significantly influences the gas-phase abundance of more complex molecules, as discussed below.

6.2. Commonly observed hot core species (b-c)

As shown by GH06, dimethyl ether, CH_3OCH_3 , methyl formate, HCOOCH_3 , and formic acid, HCOOH , are formed on the grains with abundances as great or greater than those typically observed in the gas phase, *via* the addition of heavy radicals. However, dimethyl ether and methyl formate substantially evaporate from dust grains before the majority of other, strongly-bound species. This is a result of revised binding energies, which now take into account the different structures of the isomeric radicals CH_3O and CH_2OH .

Methanol and formaldehyde are primarily formed on grains during the collapse phase, *via* CO hydrogenation. Formaldehyde is also formed early in the warm-up phase. Gas-phase methanol abundances are dictated by its grain-surface formation and subsequent co-desorption with water ice at ~ 110 K. The binding energy of formaldehyde is lower than that of methanol, resulting in its ejection from dust grains at a temperature of ~ 40 K. The injection of this large quantity of formaldehyde boosts abundances of certain gas-phase species, most notably water, methanol, and formic acid.

The injection of formaldehyde provides an abundant reaction partner for HCO^+ . This ion is the primary destruction partner for many large species, including dimethyl ether and methyl formate. In model S, the large formaldehyde abundances achieved at ~ 40 K do not last to the higher temperatures at which dimethyl ether and methyl formate evaporate, hence the survival of these species is curtailed as they are exposed to large HCO^+ abundances.

Following the evaporation of methanol, large amounts of dimethyl ether are formed in the gas phase, in spite of the low formation efficiency. The long-timescale run (model S) shows an increase in gas-phase methyl formate abundance at around 100 – 110 K. CH_3O , produced by CR-induced photodissociation of gas-phase methanol, accretes onto grains, where it may react with the strongly-bound formamide, NH_2CHO , to produce methyl formate, which then quickly evaporates. When formamide co-desorbs with H_2O , the methyl formate formation route becomes weak.

Formic acid is produced in large quantities on the grains, but also in the gas phase following the evaporation of formaldehyde, *via* $\text{OH} + \text{H}_2\text{CO} \rightarrow \text{HCOOH} + \text{H}$. The formic acid produced in the gas phase accretes onto the grains, substantially increasing grain-surface abundances. Formic acid has a large binding energy, and in the longer timescale models (M and S) its surface abundance is diminished by hydrogen abstraction by OH prior to evaporation into the gas phase. Co-desorption of formic acid with H_2O results in large abundances at high temperatures. These abundances are somewhat sustained by the gas-phase reaction of OH and formaldehyde shown above, and by $\text{HCO}^+ + \text{H}_2\text{O} \rightarrow \text{CH}_3\text{O}_2^+$ followed by recombination.

Ethanol, $\text{C}_2\text{H}_5\text{OH}$, and glycolaldehyde, $\text{CH}_2(\text{OH})\text{CHO}$, are both formed on grain surfaces in this model, mainly by addition of CH_3 and HCO to CH_2OH ; hence their grain-surface behaviour is similar to that of their structural isomers, dimethyl ether and methyl formate, respectively (acetic acid has a more complex formation route, as seen below). The CH_3 -bearing species, ethanol and dimethyl ether, are each more prevalent on the grains than their related HCO -bearing isomers, resulting from the greater prevalence of CH_3 -precursor ices. Ethanol and glycolaldehyde remain on the grains after their structural isomers have evaporated, co-desorbing with water. The retention of glycolaldehyde allows it to be destroyed by OH radicals at high temperatures, prior to complete evaporation; this is especially true for model S. The resultant $\text{CH}_2(\text{OH})\text{CO}$ radical may attach to heavier radicals at these times. In model S, CR-induced photodissociation of ethanol and glycolaldehyde on the grains becomes significant. The primary destruction processes for gas-phase ethanol and glycolaldehyde are ion–molecule reactions resulting in proton addition, followed by dissociative recombination.

Acetaldehyde, CH_3CHO , is formed on grains by the addition of CH_3 and HCO ; the mobility of CH_3 dominates grain surface formation because the barrier to HCO diffusion is somewhat higher. As for most other species, longer warm-up timescales provide longer periods over which temperatures are tuned for efficient production. Acetaldehyde reaches its peak surface abundance at ~ 30 K, and this abundance remains static until evaporation becomes strong at ~ 50 K. In model S, acetaldehyde is also produced in the gas phase at late times. The longer timescale allows more hydrocarbons to build up on the grains (see Garrod et al. 2007), and once they are released into the gas phase, acetaldehyde can form *via* $\text{C}_2\text{H}_5 + \text{O} \rightarrow \text{CH}_3\text{CHO} + \text{H}$.

Ketene, CH_2CO , is formed on grains in significant quantities during the collapse phase, primarily by repetitive hydrogenation of accreted C_2O . Later, reaction with accreted C_2 molecules, followed by hydrogenation, leads to greater surface ketene abundances prior to evaporation at ~ 40 K. Survival of gas-phase ketene is dependent on the abundance of formaldehyde in the gas phase.

Although no new CN surface chemistry has been added, the network includes the reaction $\text{CH}_3 + \text{CN} \rightarrow \text{CH}_3\text{CN}$. This is the strongest route for the formation of methyl cyanide, CH_3CN . It is also formed at earlier times by the hydrogenation of C_2N on grains. Gas-phase formation takes place following the evaporation of HCN , which reacts with CH_3^+ , producing modest methyl cyanide abundances. However, the greatest gas-phase abundance occurs upon its evaporation at ~ 90 K.

6.3. Nitrogen-bearing species (d)

Methylamine, CH_3NH_2 , is formed by simple addition of CH_3 to NH_2 on grains, and until its evaporation it is only appreciably destroyed by CR-induced photodissociation. NH_2OH is formed initially by $\text{NH} + \text{OH}$ addition on grains, followed by hydrogenation; however, as OH also becomes mobile, the addition reaction $\text{OH} + \text{NH}_2 \rightarrow \text{NH}_2\text{OH}$ becomes dominant.

HNCO is only abundant in the gas phase as a result of the destruction of larger complex species; in particular, urea, $(\text{NH}_2)_2\text{CO}$, due to its high abundance in this model, especially for longer timescales. Gas-phase production mechanisms for HNCO which are not dependent on the destruction of larger, grain surface-produced species are not included here. Nevertheless, HNCO is formed on grain surfaces by hydrogenation of accreted OCN , but is further hydrogenated to formamide, NH_2CHO , such that its abundance is very small.

HCN is formed primarily at low temperatures, beginning in the collapse phase. Gas-phase produced HCN may accrete; or, accreted gas phase-produced CN may be hydrogenated on grain surfaces. This material evaporates at ~ 40 K, and survives while formaldehyde is present in the gas phase to reduce ion abundances. At such temperatures, HCN and CN are formed by CR-induced photodissociation of CH_3CN , and both quickly evaporate. Later, following evaporation of NH_3 from grains, HCN is formed in the gas phase *via* $\text{C} + \text{NH}_2 \rightarrow \text{HCN} + \text{H}$. The behavior and abundance of HNC (not shown in Figures) are very similar to those of HCN .

Formamide, NH_2CHO , is formed on grains at low temperatures by hydrogenation of accreted OCN . It is later formed in the gas phase by the reaction of formaldehyde and NH_2 after formaldehyde evaporates at ~ 40 K. Accretion of this material leads to increased grain-surface abundances. As HCO becomes mobile on the grains, formamide is also formed by addition to NH_2 radicals. In model S, grain-surface formamide is destroyed by hydrogen abstraction, prior to evaporation. At high temperatures, formamide continues to be formed in the gas phase from NH_2 .

Following the evaporation of formaldehyde, formamide becomes an important contributor of HCO radicals, *via* its CR-induced photodissociation. A similar process occurs for CH_3 production from methylamine. In this way, these larger species formed at early times become repositories for important simple radicals until late times and high temperatures.

6.4. Complex oxygen-bearing species formed from CH_3CO (e)

Many complex molecules form from secondary radicals, which are the products of hydrogen-abstraction reactions or CR-induced photodissociation. One such radical is CH_3CO , which is the precursor to several commonly-observed hot-core molecules.

Acetone, $(\text{CH}_3)_2\text{CO}$, is formed by addition of CH_3 to CH_3CO . At the time that CH_3 becomes mobile, CH_3CO is primarily formed by hydrogen abstraction from acetaldehyde. The interpolated value for the binding energy of acetone used here is relatively low, and it evaporates at around 65 K. In this way, it behaves similarly to methyl formate and dimethyl ether, requiring ion abundances to be limited by formaldehyde for its gas-phase survival. Shorter evolutionary timescales allow its gas-phase abundance to be sustained to greater temperatures.

Acetamide, CH_3CONH_2 , is formed mainly by addition of grain-surface CH_3 to HNCO , followed by hydrogenation. Its production is increased when formaldehyde evaporates; reaction of HCO^+ with H_2CO produces more gas-phase OH and this results in faster formation of OCN. This molecule is accreted and hydrogenated on grains, to make HNCO , which may react to produce acetamide.

Acetic acid, CH_3COOH , is formed from the addition of OH to CH_3CO . This formation mechanism differentiates it from its structural isomers methyl formate and glycolaldehyde, which form from the reaction of two primary radicals. Here, the mobility of the CH_3CO radical dominates that of OH. However, at the time that CH_3CO becomes mobile, most grain-surface acetaldehyde has evaporated, and the major source of CH_3CO radicals is the CR-induced photodissociation of acetamide.

In addition to these previously observed species, two additional molecules form from similar reactions involving CH_3CO . Hydroxyacetone, $\text{CH}_2(\text{OH})\text{COCH}_3$, is formed from reaction between CH_3CO and CH_2OH , at rates determined by CH_3CO mobility. Methyl acetate, $\text{CH}_3\text{OCOCH}_3$, is formed by addition of CH_3O and CH_3CO ; these radicals become mobile at similar temperatures, and so they are both capable of reacting with stationary radicals, reducing methyl acetate production. Methyl acetate also evaporates before the majority of the ices, leaving it exposed to gas-phase ion–molecule reactions.

6.5. Complex oxygen-bearing species formed from CH_3O and CH_2OH (f – g)

Several complex species arising from CH_3O and CH_2OH form entirely on grain surfaces. Methoxymethanol, $\text{CH}_3\text{OCH}_2\text{OH}$, and dimethyl peroxide, $(\text{CH}_3\text{O})_2$, are dependent on the

mobility of the CH_3O radical. Methoxymethanol achieves greater abundances than dimethyl peroxide, as the increasing mobility (and therefore, reactivity) of the CH_3O radical reduces its abundance on grains.

Methoxyamine, CH_3ONH_2 , and hydroxymethylamine, $\text{CH}_2(\text{OH})\text{NH}_2$, are both formed around the same time as methoxymethanol and dimethyl peroxide. The NH_2 radical is still immobile at these times, but NH has a similar binding energy to CH_3O and is therefore mobile. So while methoxyamine is predominantly formed *via* direct addition of CH_3O and NH_2 radicals, hydroxymethylamine is formed by addition of NH to CH_2OH , followed by hydrogenation. Later, the NH_2 radical becomes mobile, and contributes to the formation of both species. Abundances of NH -radical-bearing species are typically $< 10^{-12}n_H$, and are therefore not shown.

Ethylene glycol, $(\text{CH}_2\text{OH})_2$, is formed far later than its structural isomers; its precursor radical, CH_2OH , becomes mobile just as water and other species are beginning to desorb. The grain-surface ethylene glycol abundance rises dramatically at ~ 110 K, and even as it begins to desorb strongly and the grain-surface abundance falls, it is still being formed in this manner. The large gas-phase quantities of ethylene glycol at late times arise from reactions on the bare grain surfaces.

The structural isomers dimethyl carbonate, $(\text{CH}_3\text{O})_2\text{CO}$, and methyl glycolate, $\text{CH}_3\text{OCOCH}_2\text{OH}$, are formed primarily by the addition of CH_3O to the secondary radicals CH_3OCO and $\text{CH}_2(\text{OH})\text{CO}$, respectively. CH_2OH addition to CH_3OCO also becomes important at later times. The production of the precursor radicals CH_3OCO and $\text{CH}_2(\text{OH})\text{CO}$ is more complex. The high gas-phase abundances of these species at late times are the result of the protonation and dissociative recombination of larger species following their evaporation from the grains. When CH_3O becomes mobile, $\text{CH}_2(\text{OH})\text{CO}$ is mainly formed *via* hydrogen-atom abstraction from glycolaldehyde by OH radicals. However, the evaporation of methyl formate precludes the analogous formation of CH_3OCO radicals. Instead, CR -induced photodissociation of methyl ester carbamic acid, $\text{CH}_3\text{OCONH}_2$, is the strongest source. The other structural isomer of dimethyl carbonate and methyl glycolate, dihydroxyacetone, $(\text{CH}_2\text{OH})_2\text{CO}$, is formed when CH_2OH becomes mobile on the grains, and therefore behaves similarly to ethylene glycol.

6.6. Other complex organics (h – j)

A variety of even more complex organic molecules form in this reaction network. Methyl carbamate, $\text{CH}_3\text{OCONH}_2$, glycolamide, $\text{CH}_2(\text{OH})\text{CONH}_2$, urea, $(\text{NH}_2)_2\text{CO}$, and carbamic

acid, NH_2COOH , are all formed as HNCO becomes mobile at around 40 – 50 K. HNCO reacts with CH_3O , CH_2OH , NH , and OH , the products of which may be hydrogenated to form the saturated species. The final up-turn in the abundances of these species is the result of primary-radical addition to NH_2CO . This species is formed by hydrogen abstraction from formamide; hence the abundances of the four species strongly correlate with that of acetamide. Carbamic acid also benefits at late times from the addition of NH_2 to COOH .

The OH radical readily reacts with several primary and secondary radicals to form other complex organics. The methanol derivatives react with OH to form methyl peroxide, CH_3OOH , and methanediol, $\text{CH}_2(\text{OH})_2$. The high mobility of both CH_3O and OH as temperature increases disfavors methyl peroxide formation, as each radical becomes scarce. Methanediol production does not suffer in this way.

Species containing carboxylic acid groups are also formed on grain surfaces. Carbonic acid, HOCOOH , methyl carbonate, CH_3OCOOH , and glycolic acid, $\text{CH}_2(\text{OH})\text{COOH}$, all require hydrogen abstraction from the aldehyde functional groups of other complex molecules to form their pre-cursor radicals, hence they are formed on the grains at late times. It is possible that these molecules can undergo further esterification reactions, though this type of chemistry has not been included in the network.

6.7. Products of polymerization reactions (j – k)

Many species are formed by addition of the important primary radicals to other primary radicals of the same type. In the case of $\text{HCO} + \text{HCO}$, the resultant OHCCHO molecule can undergo hydrogen abstraction to form the COCHO radical, which can then react with primary radicals to form a variety of complex species. Several more complex species involving $-\text{COCHO}$ groups are also formed from reactions involving other secondary radicals and HCO . This type of CO -polymerization chemistry can quickly lead to a high level of molecular complexity, and so this chemistry was limited to molecules with $-\text{COCHO}$ groups. Therefore, molecules with a $-\text{CO}(\text{CO})\text{CHO}$ backbone or larger are not included in the network.

Several highly abundant simple species are also formed from this type of chemistry. Ethane, C_2H_6 and hydrogen peroxide, H_2O_2 , were present in previous versions of the rate-file, while hydrazine, $(\text{NH}_2)_2$, is a new addition. In spite of the new formation mechanism introduced, C_2H_6 is formed predominantly throughout the warm-up phase by hydrogenation of C_2H_4 , which is accreted from the gas phase. C_2H_4 is formed *via* $\text{CH}_4 + \text{CH} \rightarrow \text{C}_2\text{H}_4 + \text{H}$, fed by the evaporation of CH_4 from the grain surfaces. Hydrogen peroxide is formed initially by the hydrogenation of molecular oxygen, but is later strongly enhanced in abundance when

OH becomes mobile. Hydrazine is formed mainly by the addition of NH to NH₂ radicals, followed by hydrogenation, and at a late stage by direct addition of NH₂ radicals. The abundance of each of these three species is fairly robust to changing evolutionary timescales.

REFERENCES

- Aikawa, Y., Wakelam, V., Garrod, R. T. & Herbst, E. 2008, *ApJ*, 674, 984
- Allen, M. & Robinson, G. W. 1977, *ApJ*, 212, 396
- Apponi, A. J., Halfen, D. T., Ziurys, L. M., Hollis, J. M., Remijan, A. J. & Lovas, F. J. 2006, *ApJ*, 643, L29
- Bisschop, S. E., Jørgensen, J. K., van Dishoeck, E. F. & de Wachter, E. B. M. 2007, *A&A*, 465, 913
- Boogert, A. C. A., Blake, G. A. & Öberg, K. 2004, *ApJ*, 615, 344
- Boogert, A. C. A., Pontoppidan, K. M., Knez, C., Lahuis, F., Kessler-Silacci, J., van Dishoeck, E. F., Blake, G. A., Augereau, J.-C., Bisschop, S. E., Bottinelli, S., Brooke, T. Y., Brown, J., Crapsi, A., Evans, N. J. II, Fraser, H. J., Geers, V., Huard, T. L., Jørgensen, J. K., Öberg, K., Allen, L. E., Harvey, P. M., Koerner, D. W., Mundy, L. G., Padgett, D. L., Sargent, A. I. & Stapelfeldt, K. R. 2008, *ApJ*, accepted
- Bottinelli, S., Ceccarelli, C., Lefloch, B., Williams, J. P., Castets, A., Caux, E., Cazaux, S., Maret, S., Parise, B. & Tielens, A. G. G. M. 2004, *ApJ*, 615, 354
- Bottinelli, S., Ceccarelli, C., Neri, R., Williams, J. P., Caux, E., Cazaux, S., Lefloch, B., Maret, S. & Tielens, A. G. G. M. 2004, *ApJ*, 617, L69
- Bottinelli, S., Ceccarelli, Williams, J. P. & Lefloch, B. 2007, *A&A*, 463, 601
- Caselli, P., Hasegawa, T. I., Herbst, E. 1998, *ApJ*, 408, 548
- Cazaux, S., Tielens, A. G. G. M., Ceccarelli, C., Castets, C., Wakelam, V., Caux, E., Parise, B. & Teyssier, D. 2003, *ApJ*, 593, L51
- Chang A. H. H. & Lin S. H., 2002, *Chem. Phys. Lett.*, 363, 175
- Chang A. H. H. & Lin S. H., 2004, *Chem. Phys. Lett.*, 384, 229
- Charnley, S. B., Kress, M. E., Tielens, A. G. G. M. & Millar, T. J. 1995, *ApJ*, 448, 232

- Collings, M. P., Anderson, M. A., Chen, R., Dever, J. W., McCoustra, M. R. S. & Williams, D. A. 2004, MNRAS, 354, 1133
- Friedel, D. N., Snyder, L. E., Remijan, A. J. & Turner, B. E. 2005, ApJ, 632, L95
- Friedel, D. N. & Snyder, L. E. 2008, ApJ, 672, 962 ,
- Garrod, R. T., Park, I.-H., Caselli, P. & Herbst, E. 2006, Faraday Discuss., 133, 51
- Garrod, R. T. & Herbst, E. 2006, A&A, 457, 927 (GH06)
- Garrod, R. T., Wakelam, V. & Herbst, E. 2007, A&A, 467, 1103
- Geppert, W. D., Hamberg, M., Thomas, R. D., Österdahl, F., Hellberg, F., Zhaunerchyk, V., Ehlerding, A., Millar, T. J., Roberts, H., Semaniak, J., af Ugglas, M., Källberg, A., Simonsson, A., Kaminska, M. & Larsson, M. 2006, in *Chemical Evolution of the Universe*, Faraday Discussions, 133, 177
- Gibb, E. L., Whittet, D. C. B., Schutte, W. A., Boogert, A. C. A., Chiar, J. E., Ehrenfreund, P., Gerakines, P. A., Keane, J. V., Tielens, A. G. G. M., van Dishoeck, E. F. & Kerkhof, O. 2000, ApJ, 536, 347
- Gibb, E. L., Whittet, D. C. B., Boogert, A. C. A., & Tielens, A. G. G. M. 2004, ApJS, 151, 35
- Graedel, T. E., Langer, W. D. & Frerking, M. A. 1982, ApJS, 48, 321
- Gredel, R., Lepp, S., Dalgarno, A. & Herbst, E. 1989, ApJ, 347, 289
- Hasegawa, T. & Herbst, E. 1992, ApJS, 82, 167
- Herbst, E., Green, S., Thaddeus, P., & Klemperer, W. 1977, ApJ, 215, 503
- Herbst, E. & Leung, C. M. 1986, ApJ, 310, 378
- Hippler, H. & Viskolcz, B. 2002, *Phys. Chem. Chem. Phys.*, 4, 4663
- Hollis, J. M., Lovas, F. J. & Jewell, P. R. 2000, ApJ, 540, L107
- Hollis, J. M. & Churchwell, E. 2001, ApJ, 551, 803
- Hollis, J. M., Vogel, S. N., Snyder, L. E., Jewell, P. R. & Lovas, F. J. 2001, ApJ, 554, 81
- Hollis, J. M., Lovas, F. J., Jewell, P. R. & Coudert, L. H. 2002, ApJ, 571, L59

- Hollis, J. M., Jewell, P. R., Lovas, F. J. & Remijan, A. 2004, *ApJ*, 613, 45
- Hollis, J. M., Lovas, F. J., Remijan, A., Jewell, P. R., Ilyushin, V. V. & Kleiner, I. 2006, *ApJ*, 643, L25
- Horn, A., Møllendal, H., Sekiguchi, O., Uggerud, E., Roberts, H., Herbst, E., Viggiano, A. A. & Fridgen, T. D. 2004, *ApJ*, 611, 605
- Katz, N., Furman, I., Biham, O., Pirronello, V. & Vidali, G. 1999, *ApJ*, 522, 305
- Kroes, G. J. & Andersson, S. 2006, *IAU Symposium*, 231, 427
- Lee, H.-H., Herbst, E., Pineau des Fôrets, G., Roueff, E. & Le Bourlot, J. 1996, *A&A*, 311, 690
- Liu, S.-Y., Mehringer, D. M. & Snyder, L. E. 2001, *ApJ*, 552, 654
- Millar, P. J., Herbst, E. & Charnley, S. B. 1991, *ApJ*, 369, 147
- NIST Computational Chemistry Comparison and Benchmark Database 2005, NIST Standard Reference Database Number 101 Release 12, Editor: Russell D. Johnson III, <http://srdata.nist.gov/cccbdb>
- Nummelin, A., Bergman, P. & Hjalmarsen, Å, 2000, *ApJ*, 128, 213
- Peeters, Z., Rodgers, S. D., Charnley, S. B., Schriver-Mazzuoli, L., Schriver, A., Keane, J. V. & Ehrenfreund, P. 2006, *A&A*, 445, 197
- Ponomarev, D. & Takhistov, V. 2005, *Internet Electron. J. Mol. Des.*, 4, 367, <http://www.biochempress.com>
- Redman, M. P., Rawlings, J. M. C., Nutter, D. J., Ward-Thompson, D. & Williams, D. A. 2002, *MNRAS*, 337, L17
- Remijan, A., Snyder, L. E., Liu, S.-Y., Mehringer, D., & Kuan, Y.-J. 2002, *ApJ*, 576, 264
- Remijan, A., & Hollis, J. M. 2006, *ApJ*, 640, 842
- Ruffle, D. P. & Herbst, E. 2000, *MNRAS*, 319, 837
- Ruffle, D. P. & Herbst, E. 2001, *MNRAS*, 322, 770
- Ruffle, D. P. & Herbst, E. 2001, *MNRAS*, 324, 1054
- Schöier, F. L., Jørgensen, J. K., van Dishoeck, E. F., & Blake, G. A. 2002, 390, 1001

Shalabiea, O. M., Caselli, P. & Herbst, E. 1998, ApJ, 502, 652

Snyder, L. E., Lovas, F. J., Mehringer, D. M., Miao, N. Y., Kuan, Y.-J., Hollis, J. M. & Jewell, P. R. 2002, ApJ, 578, 245

van der Tak, F. F. S., van Dishoeck, E. F. & Caselli, P. 2000, A&A, 361, 327

van Dishoeck, E.F. & Blake, G. A. 1998 *Annual Review of Astronomy and Astrophysics*, 36, 317

Viti, S., Collings, M. P., Dever, J. W., McCoustra, M., R. S. & Williams, D. A. 2004, MNRAS, 354, 1141

Woon, D. E. 2002, ApJ, 569, 541

E_b (K)	225	557	588	800	1189	1250	1425	1978	2254
Radical	H	CO	CH ₃	HCO	NH	CH ₃ O	OH	NH ₂	CH ₂ OH
H	H ₂								
CO	HCO	x							
CH ₃	CH ₄	CH ₃ CO	C ₂ H ₆						
HCO	H ₂ CO	x	CH ₃ CHO	OHCCCHO					
NH	NH ₂	HNCO	CH ₃ NH	HNCHO	N ₂ H ₂				
CH ₃ O	CH ₃ OH	CH ₃ OCO	CH ₃ OCH ₃	HCOOCH ₃	CH ₃ ONH	(CH ₃ O) ₂			
OH	H ₂ O	COOH (CO ₂ + H)	CH ₃ OH	HCOOH	HNOH	CH ₃ OOH	H ₂ O ₂		
NH ₂	NH ₃	NH ₂ CO	CH ₃ NH ₂	NH ₂ CHO	HNNH ₂	CH ₃ ONH ₂	NH ₂ OH	(NH ₂) ₂	
CH ₂ OH	CH ₃ OH	CH ₂ (OH)CO	C ₂ H ₅ OH	CH ₂ (OH)CHO	CH ₂ (OH)NH	CH ₃ OCH ₂ OH	CH ₂ (OH) ₂	CH ₂ (OH)NH ₂	(CH ₂ OH) ₂
E_A (K)	2500	1500 (80)							

Fig. 1.— Primary radical–primary radical reactions. Radicals are arranged in order of increasing diffusion energy barrier (shown in the top row). The product of each reaction is shown in the box corresponding to the pair of reactants; ‘x’ signifies reactions excluded from the reaction set. Darker product boxes signify reactions with activation energies, and the values are indicated at the bottom of each column.

E_b (K)		225	588	800	1189	1250	1425	1978	2254
Radical	H	CH ₃	HCO	NH	CH ₃ O	OH	NH ₂	CH ₂ OH	
1163	CH ₃ CO	CH ₃ CHO	CH ₃ COCH ₃	CH ₃ COCHO	CH ₂ CONH	CH ₃ OCOCH ₃	CH ₃ COOH	CH ₃ CONH ₂	CH ₃ COCH ₂ OH
1375	COCHO	OHCCCHO	CH ₃ COCHO	HCOCOCHO	HNCOCHO	CH ₃ OCOCHO	OHCCOOH	CH ₂ (OH)NH ₂	CH ₂ (OH)COCHO
1425	HNCO	HNCHO NH ₂ CO	CH ₃ CONH	HNCOCHO	HNCONH	CH ₃ OCONH	HNCCOOH	NH ₂ CONH	CH ₂ (OH)CONH
1777	CH ₃ NH	CH ₃ NH ₂	x	x	x	x	x	x	x
1800	CH ₃ OCO	HCOOCH ₃	CH ₃ OCOCH ₃	CH ₃ OCOCHO	CH ₃ OCONH	(CH ₃ O) ₂ CO	CH ₃ OCOOH	CH ₃ OCONH ₂	CH ₃ OCOCH ₂ OH
1989	HNCHO	NH ₂ CHO	x	x	x	x	x	x	x
2378	N ₂ H ₂	N ₂ + H ₂ + H	x	x	x	x	x	x	x
2414	CH ₃ ONH	CH ₃ ONH ₂	x	x	x	x	x	x	x
2553	NH ₂ CO	NH ₂ CHO	CH ₃ CONH ₂	NH ₂ COCHO	NH ₂ CONH	CH ₃ OCONH ₂	NH ₂ COOH	(NH ₂) ₂ CO	CH ₂ (OH)CONH ₂
2560	COOH	HCOOH	CH ₃ COOH	OHCCOOH	HNCOOH	CH ₃ OCOOH	HOCCOOH	NH ₂ COOH	CH ₂ (OH)COOH
2614	HNOH	NH ₂ OH	x	x	x	x	x	x	x
3117	CH ₂ (OH)CO	CH ₂ (OH)CHO	CH ₂ (OH)COCH ₃	CH ₂ (OH)COCHO	CH ₂ (OH)CONH	CH ₃ OCH ₂ OH	CH ₂ (OH)COOH	CH ₂ (OH)CONH ₂	(CH ₂ OH) ₂ CO
3167	HNNH ₂	(NH ₂) ₂	x	x	x	x	x	x	x
3731	CH ₂ (OH)NH	CH ₂ (OH)NH ₂	x	x	x	x	x	x	x
E_A (K)	650								

Fig. 2.— Primary radical–secondary radical reactions. Primary radicals are shown along the top edge; secondary radicals on the left-hand edge. Radicals are arranged in order of increasing diffusion energy barrier (shown in the top row and the first column). The product(s) of each addition reaction is (are) shown in the box corresponding to the pair of reactants; ‘x’ signifies reactions excluded from the reaction set. Darker product boxes signify reactions with activation energies, and the values are indicated at the bottom of each column. White boxes signify reactions whose rates are dominated by the mobility of the secondary radical, i.e. $E_b(\text{primary}) > E_b(\text{secondary})$.

E_b (K)	Radical / aldehyde	225	588	1189	1250	1425	1978	2254
		H	CH ₃	NH	CH ₂ O	OH	NH ₂	CH ₂ OH
1025	H ₂ CO	CH ₂ O (2500) CH ₂ OH (2500)	CH ₄ + HCO (4450)	NH ₂ + HCO (2850)	CH ₂ OH + HCO (1500) HCOOCH ₃ + H (2850)	H ₂ O + HCO (2500) HCOOH + H (2500)	NH ₂ + HCO (2850) NH ₂ CHO + H (2850)	CH ₂ OH + HCO (2950)
1388	CH ₃ CHO	H ₂ + CH ₃ CO (2120) HCO + CH ₄ (2400) H ₂ CO + CH ₃ (2400)	CH ₄ + CH ₃ CO (3020) C ₂ H ₅ + HCO (2400)	NH ₂ + CH ₃ CO (5770)	CH ₂ OH + CH ₃ CO (2850) HCOOCH ₃ + CH ₃ (2400)	H ₂ O + CH ₃ CO (1500) CH ₂ OH + HCO (2400) HCOOH + CH ₃ (2400)	NH ₂ + CH ₃ CO (1250) CH ₂ NH ₂ + HCO (2400) NH ₂ CHO + CH ₃ (2400)	CH ₂ OH + CH ₃ CO (2850) C ₂ H ₅ OH + HCO (2400) CH ₂ (OH)CHO + CH ₃ (2400)
1600	OHCHO	H ₂ CO + HCO (2400)	CH ₃ CHO + HCO (2400)	HNCHO + HCO (2400)	HCOOCH ₃ + HCO (2400)	H ₂ O + COCHO (1500) HCOOH + HCO (2400)	NH ₂ CHO + HCO (2400)	CH ₂ (OH)CHO + HCO (2400)
2050	HCOOCH ₃	H ₂ + CH ₃ OCO (3970) CH ₂ OH + HCO (2450)	CH ₄ + CH ₃ OCO (5180)	x	CH ₂ OH + CH ₃ OCO (4120)	H ₂ O + CH ₃ OCO (1500) HCOOH + CH ₃ O (2450)	NH ₂ + CH ₃ OCO (2850)	x
2778	NH ₂ CHO	H ₂ + NH ₂ CO (9630) NH ₃ + HCO (2100)	CH ₄ + NH ₂ CO (3560)	x	CH ₂ OH + NH ₂ CO (2850) HCOOCH ₃ + NH ₂ (2100)	H ₂ O + NH ₂ CO (1500) HCOOH + NH ₂ (2100)	NH ₃ + NH ₂ CHO (2850)	CH ₂ OH + NH ₂ CO (2850)
2785	HCOOH	H ₂ + COOH (2850) HCO + H ₂ O (2450)	CH ₄ + COOH (2850)	x	CH ₂ OH + COOH (2850)	H ₂ O + COOH (1500)	NH ₂ + COOH (2850)	x
3342	CH ₂ (OH)CHO	H ₂ + CH ₂ (OH)CO (2850) CH ₂ OH + HCO (2400)	CH ₄ + CH ₂ (OH)CO (2850) C ₂ H ₅ OH + HCO (2400)	NH ₂ + CH ₂ (OH)CO (2850)	CH ₂ OH + CH ₂ (OH)CO (2850) HCOOCH ₃ + CH ₂ OH (2400)	H ₂ O + CH ₂ (OH)CO (1500) HCOOH + CH ₂ OH (2400)	NH ₂ + CH ₂ (OH)CO (2850) NH ₂ CHO + CH ₂ OH (2400)	CH ₂ OH + CH ₂ (OH)CO (2850) (CH ₂ OH) ₂ + HCO (2400)

Fig. 3.— Primary radical–aldehyde-group reactions. Primary radicals are shown along the top edge; aldehyde group-bearing species on the left-hand edge. Species are arranged in order of increasing diffusion energy barrier (given in K; see the top row and the first column). The products of each reaction are shown in the box corresponding to the pair of reactants; ‘x’ signifies reactions excluded from the reaction set. All reactions have activation energies, shown in brackets. White boxes signify reactions whose rates are dominated by the mobility of the aldehyde group-bearing species, i.e. $E_b(\text{radical}) > E_b(\text{X-CHO})$.

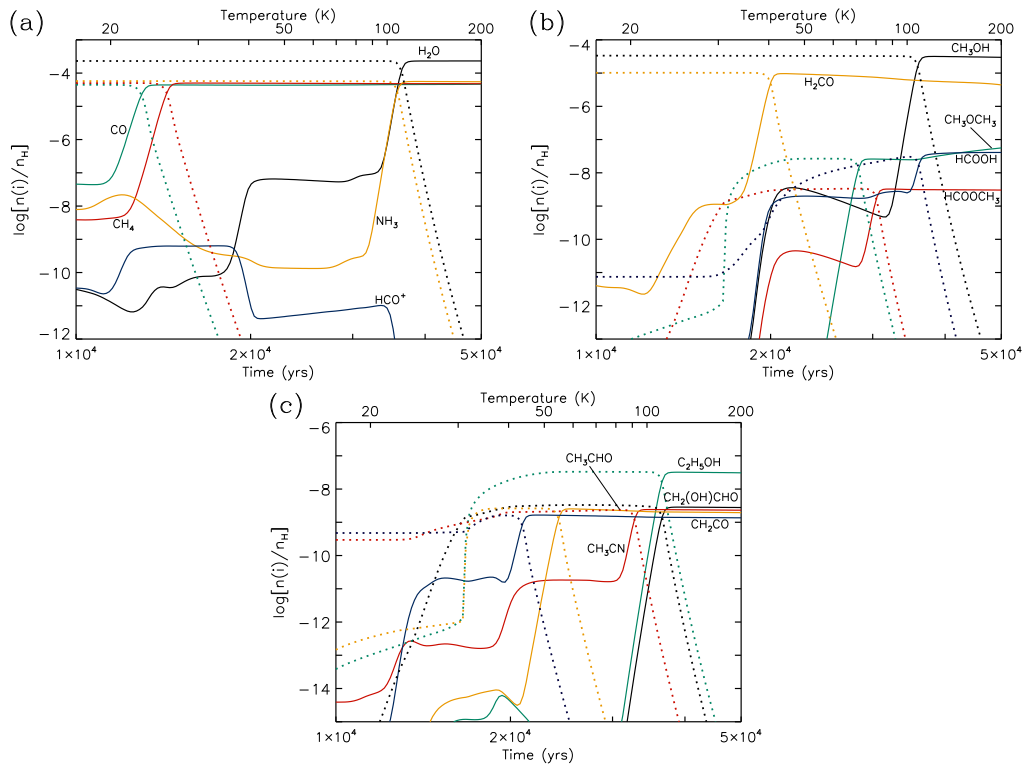
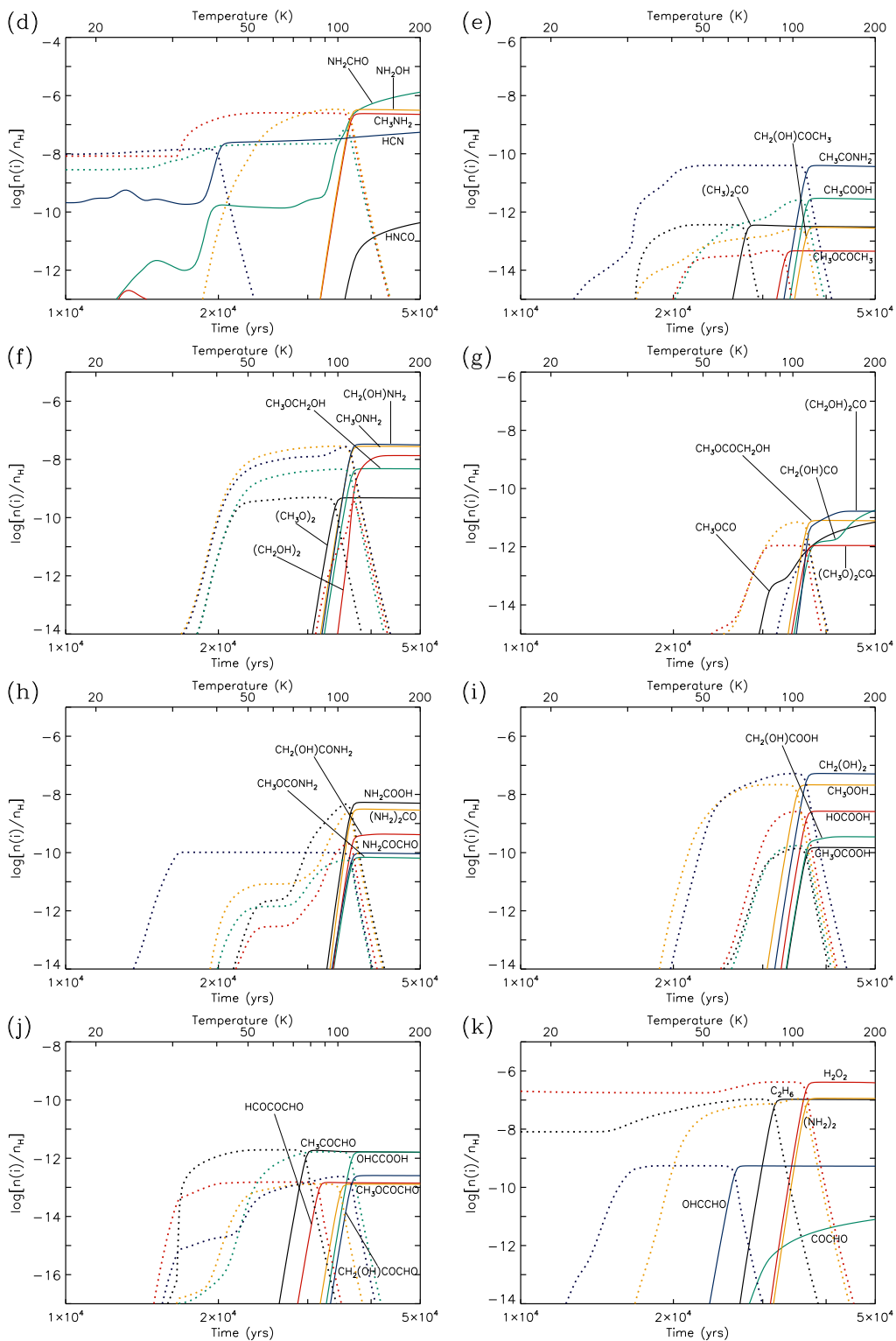


Fig. 4.— Fractional abundances for model F, with a warm-up timescale of 5×10^4 yr. Solid lines indicate gas-phase species; dotted lines of the same color indicate the grain-surface species. [See the electronic edition of the *Journal* for panels d–k.]



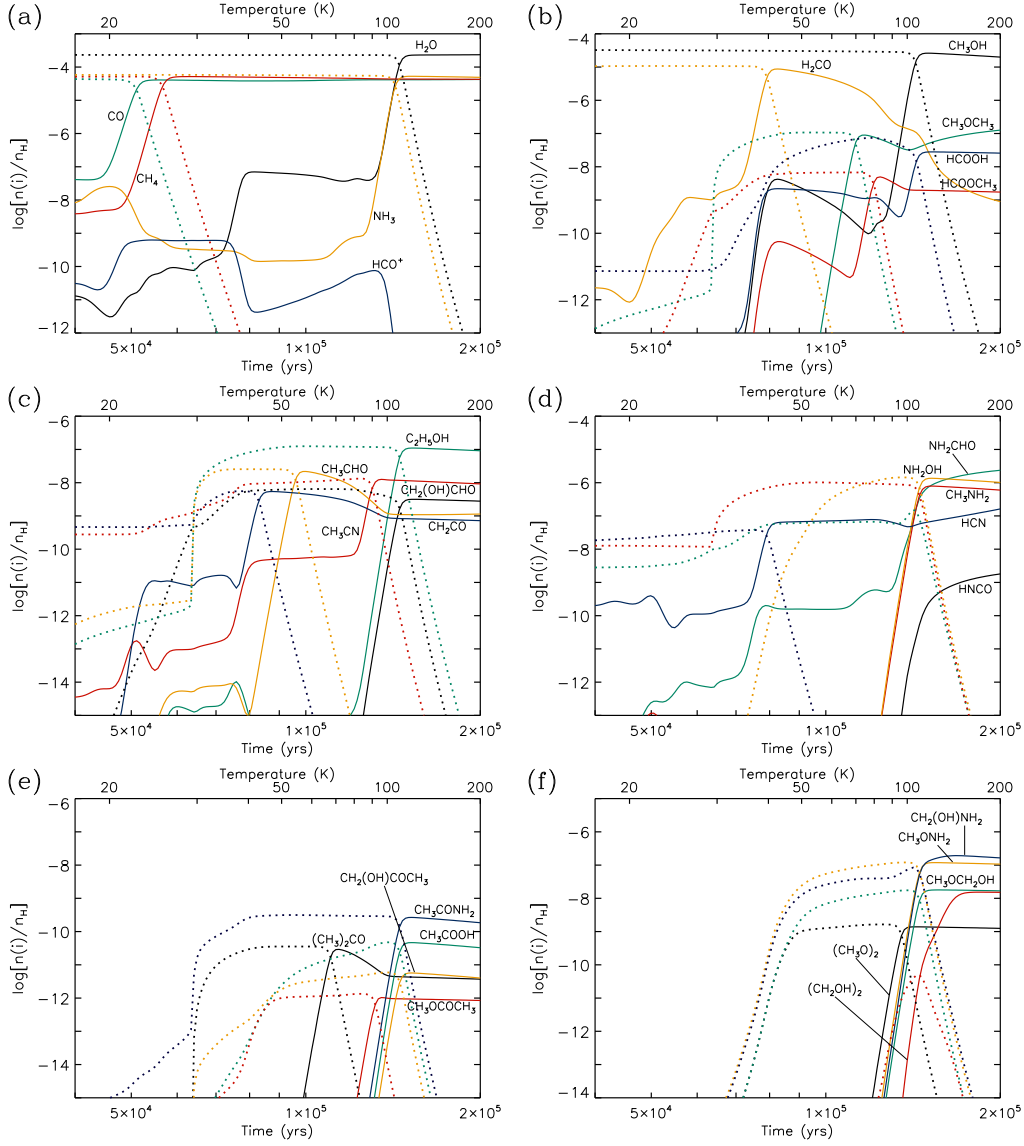
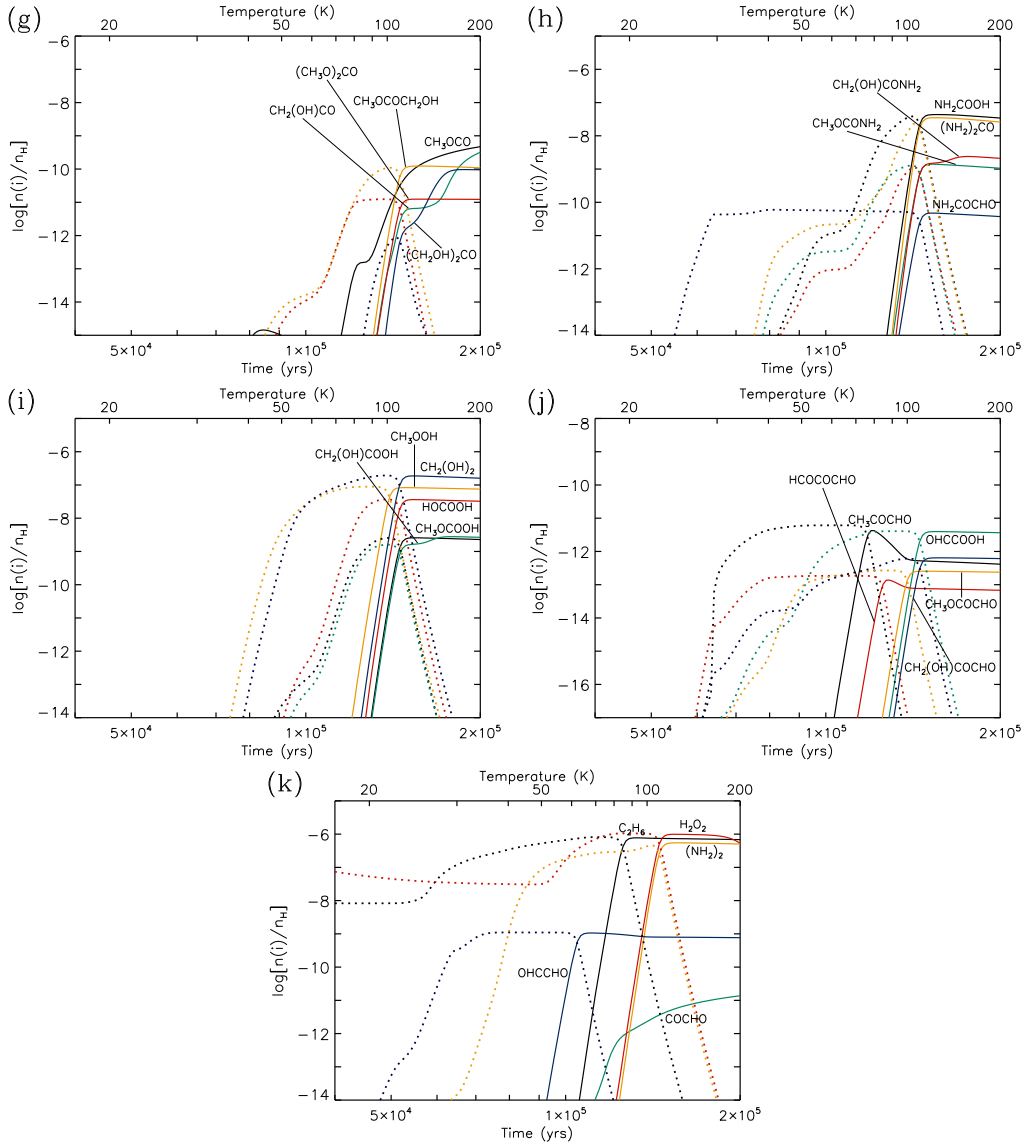


Fig. 5.— Fractional abundances for model M, with a warm-up timescale of 2×10^5 yr. Solid lines indicate gas-phase species; dotted lines of the same color indicate the grain-surface species. [See the electronic edition of the *Journal* for panels g–k.]



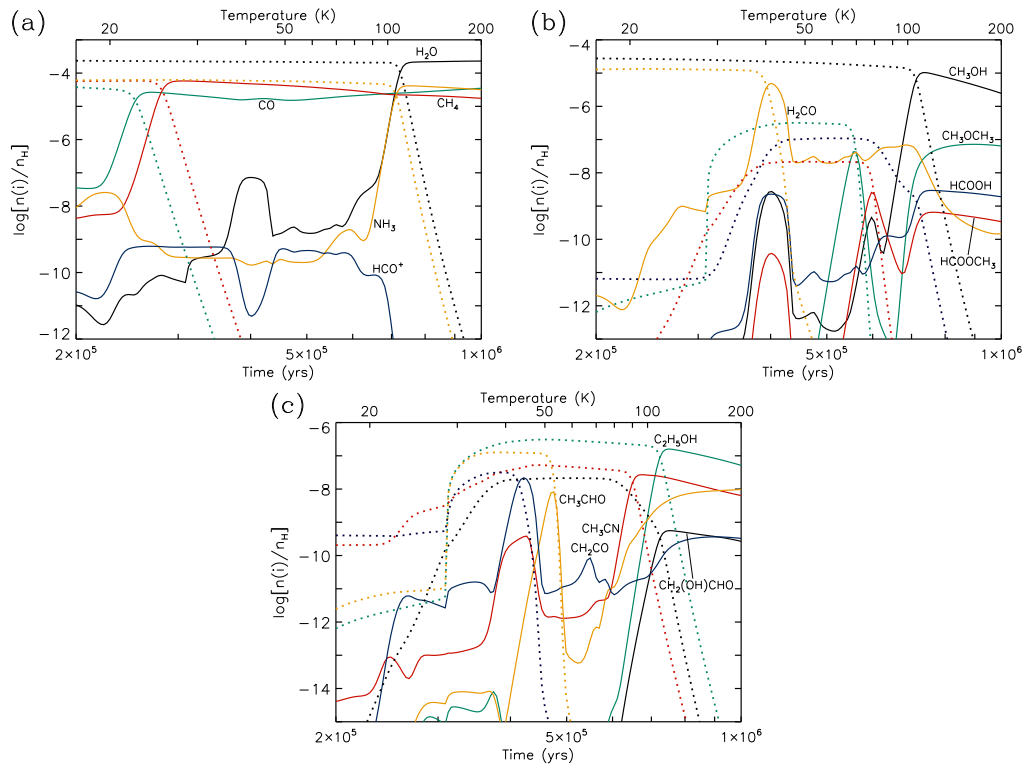
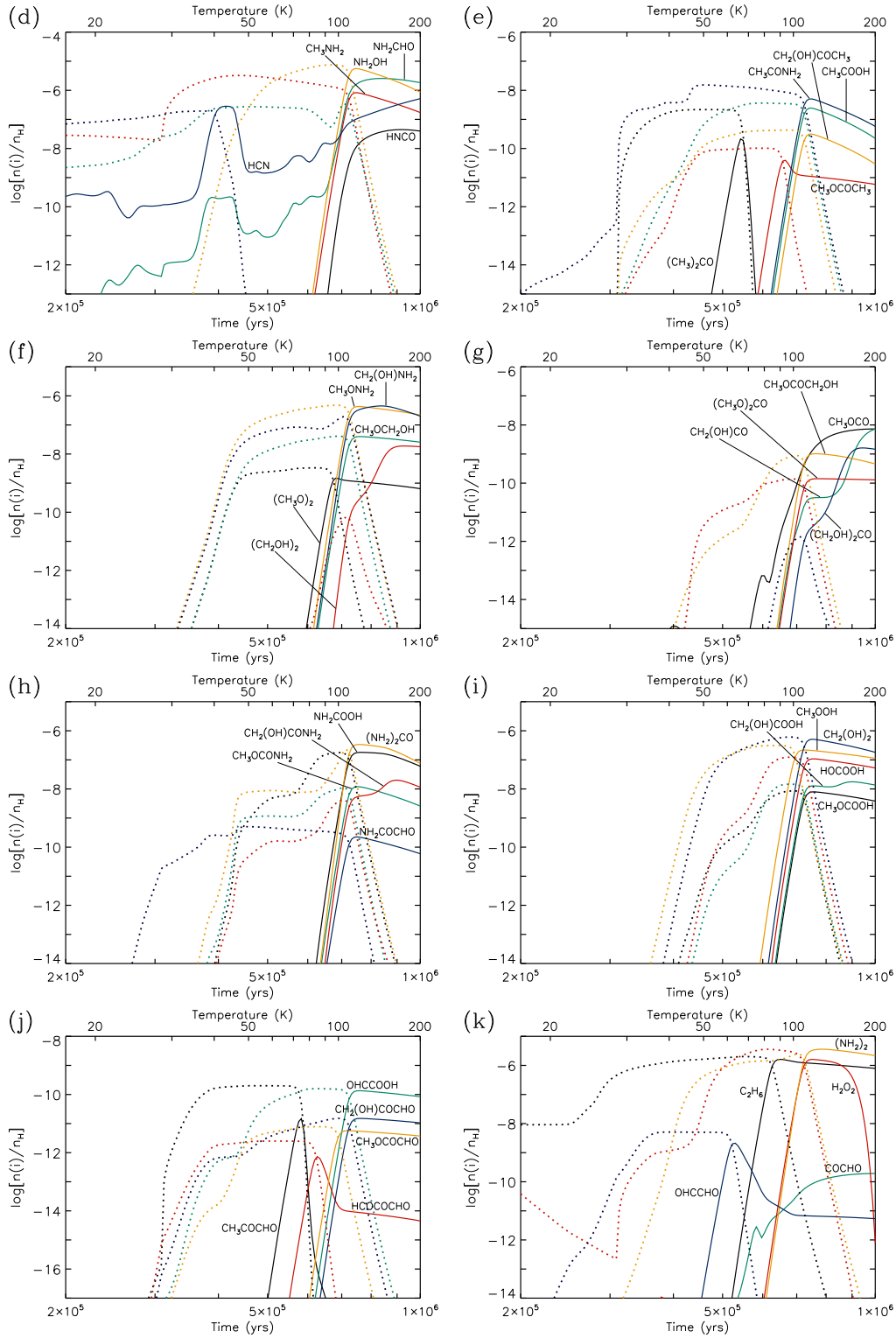


Fig. 6.— Fractional abundances for model S, with a warm-up timescale of 1×10^6 yr. Solid lines indicate gas-phase species; dotted lines of the same color indicate the grain-surface species. [See the electronic edition of the *Journal* for panels d–k.]



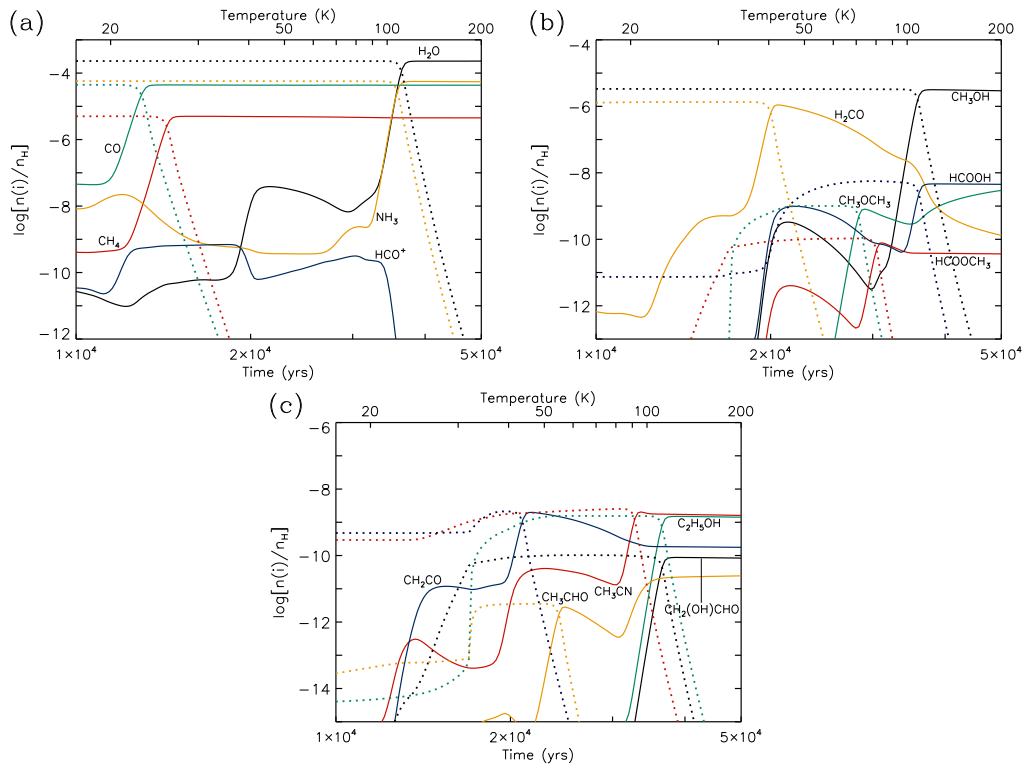
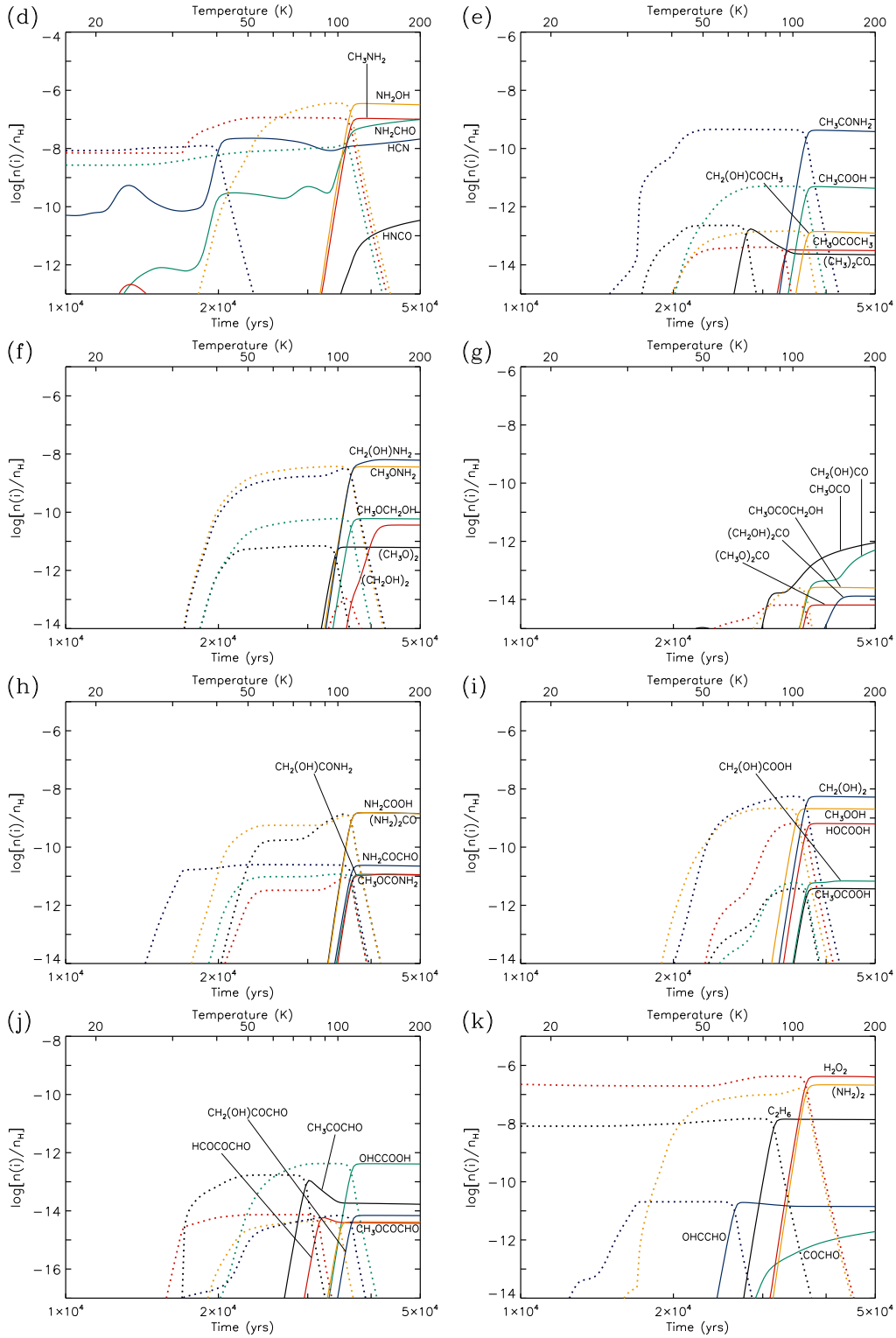


Fig. 7.— Fractional abundances for model F(ice), with a warm-up timescale of 5×10^4 yr. Solid lines indicate gas-phase species; dotted lines of the same color indicate the grain-surface species. [See the electronic edition of the Journal for panels d–k.]



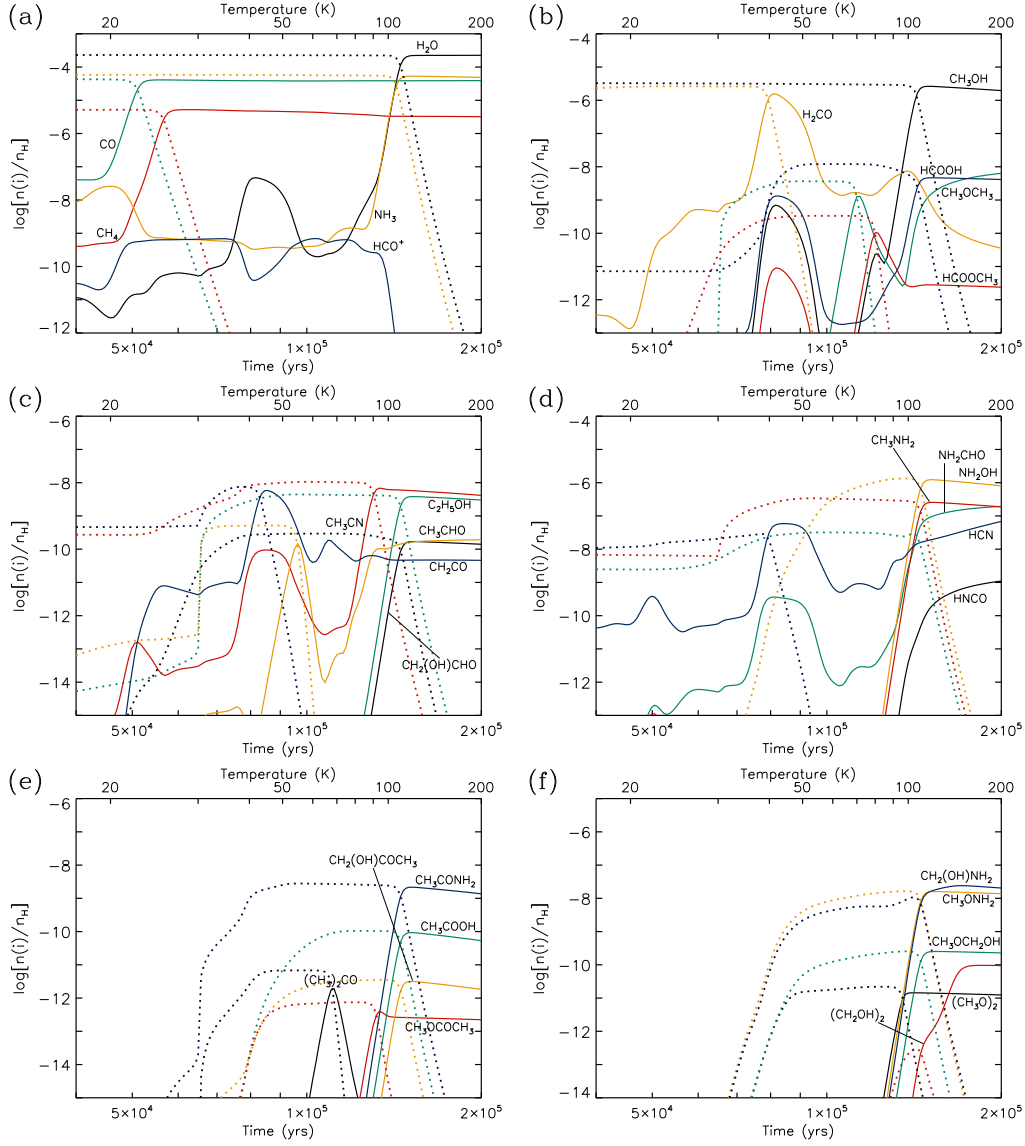
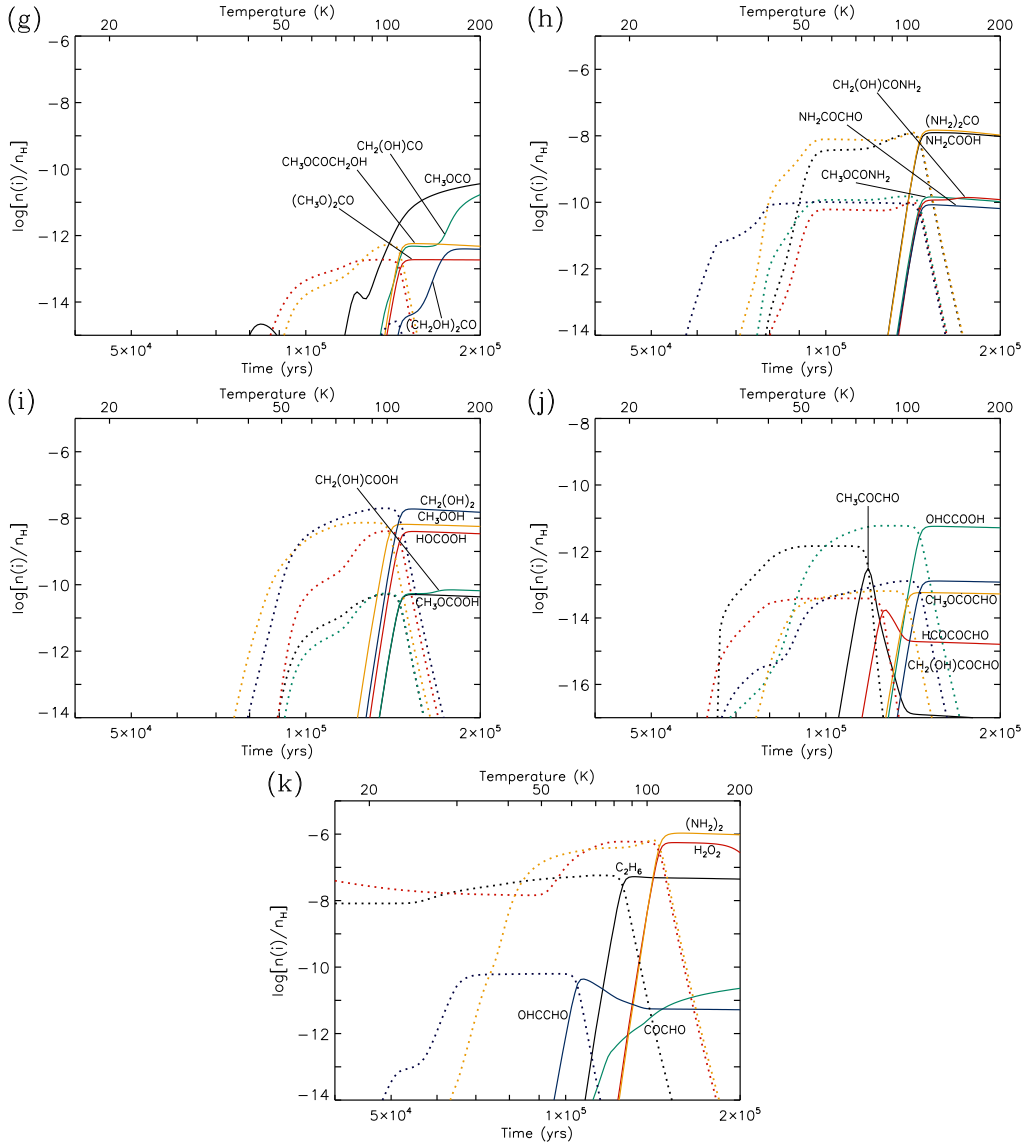


Fig. 8.— Fractional abundances for model M(ice), with a warm-up timescale of 2×10^5 yr. Solid lines indicate gas-phase species; dotted lines of the same color indicate the grain-surface species. [See the electronic edition of the *Journal* for panels g–k.]



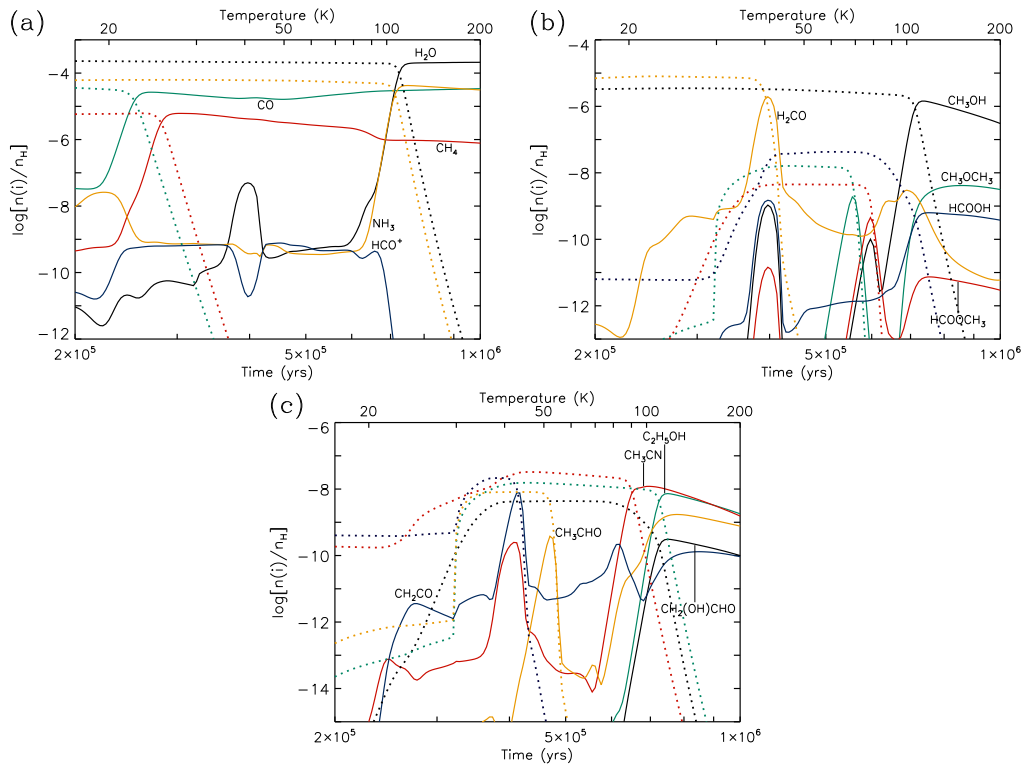


Fig. 9.— Fractional abundances for model S(ice), with a warm-up timescale of 1×10^6 yr. Solid lines indicate gas-phase species; dotted lines of the same color indicate the grain-surface species. [See the electronic edition of the *Journal* for panels d–k.]

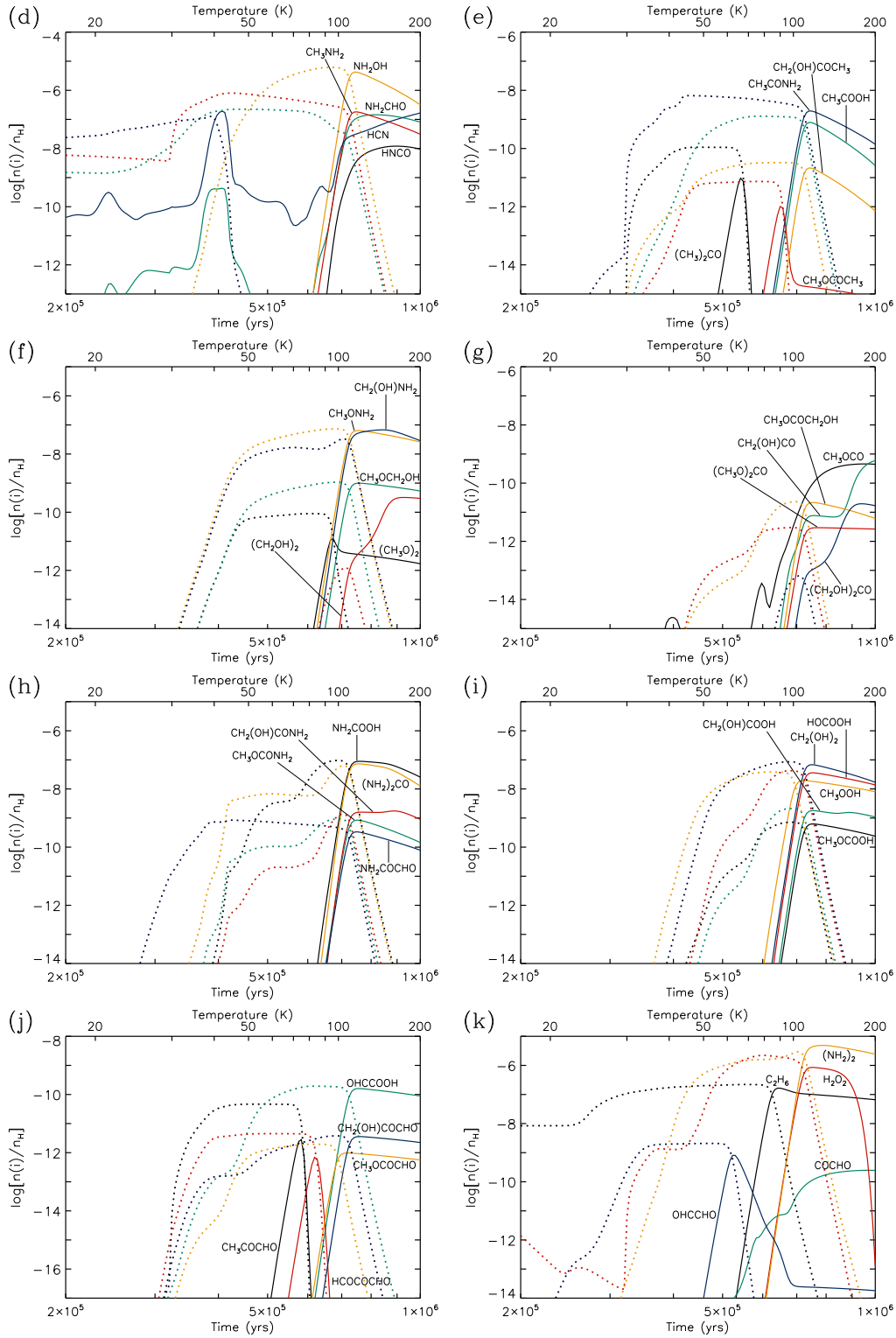


Table 1. Products and Rates of Cosmic-Ray Dissociation of Molecular Ice Species.

Species	Products	Rate multiplier, b [†]
H ₂ O	→ OH + H	970
CH ₄	→ CH ₂ + H ₂	2340
NH ₃	→ NH + H ₂	540
NH ₃	→ NH ₂ + H	1320
HCO	→ CO + H	421
H ₂ CO	→ HCO + H	1330
H ₂ CO	→ CO + H ₂	1330
CH ₃ OH	→ CH ₃ + OH	1500
CH ₃ OH	→ CH₃O + H	500
CH ₃ OH	→ CH₂OH + H	500

[†]Rate, $k = b \times \zeta$, where ζ is the cosmic-ray ionization rate.

Note. — Boldface denotes divergence from Gredel et al. (1989) products/rates.

Table 2. Initial fractional abundances, with respect to total hydrogen, of elements and H₂ at the start of the collapse phase.

Species, i	n_i/n_H [†]
H ₂	0.33
H	0.33
He	0.09
C	1.4(−4)
N	7.5(−5)
O	3.2(−4)
S	8.0(−8)
Na	2.0(−8)
Mg	7.0(−9)
Si	8.0(−9)
P	3.0(−9)
Cl	4.0(−9)
Fe	3.0(−9)

$${}^\dagger a(b) = a^b$$

Table 3. Warm-up phase model parameters

Model	Warm-up timescale (yr)	Ice composition
F	5×10^4	Standard
M	2×10^5	Standard
S	1×10^6	Standard
F(ice)	5×10^4	Reduced
M(ice)	2×10^5	Reduced
S(ice)	1×10^6	Reduced

Table 4. Peak gas-phase abundances and associated temperatures for standard warm-up phase models F, M, and S[†].

Species	Model F		Model M		Model S	
	Peak $n[i]/n_H$	T (K)	Peak $n[i]/n_H$	T (K)	Peak $n[i]/n_H$	T (K)
CO	4.6(-5)	200	4.2(-5)	200	3.5(-5)	200
H ₂ O	2.3(-4)	200	2.3(-4)	200	2.3(-4)	200
CH ₄	5.0(-5)	29	5.2(-5)	29	5.8(-5)	28
NH ₃	5.6(-5)	124	5.3(-5)	120	4.1(-5)	117
HCO ⁺	6.4(-10)	33	6.3(10)	24	6.2(-10)	24
CH ₃ OH	3.2(-5)	122	2.6(-5)	117	1.0(-5)	112
H ₂ CO	9.6(-6)	44	8.7(-6)	42	4.9(-6)	41
HCOOH	4.1(-8)	190	2.8(-8)	120	3.0(-9)	119
HCOOCH ₃	3.3(-9)	88	5.0(-9)	83	2.6(-9)	78
CH ₃ OCH ₃	5.6(-8)	200	1.3(-7)	200	7.2(-8)	163
CH ₂ (OH)CHO	2.9(-9)	127	3.2(-9)	123	5.6(-10)	117
C ₂ H ₅ OH	3.2(-8)	124	1.1(-7)	120	1.6(-7)	117
CH ₃ CHO	2.5(-9)	59	2.2(-8)	58	9.7(-9)	200
CH ₂ CO	1.7(-9)	48	5.4(-9)	46	2.2(-8)	44
CH ₃ CN	2.4(-9)	102	1.3(-8)	97	2.7(-8)	96
HCN	5.5(-8)	200	1.6(-7)	200	5.2(-7)	200
HNCO	4.3(-11)	200	1.8(-9)	200	4.5(-8)	171
NH ₂ CHO	1.3(-6)	200	2.4(-6)	200	2.6(-6)	143
CH ₃ NH ₂	2.4(-7)	124	7.9(-7)	120	8.3(-7)	117
NH ₂ OH	3.3(-7)	124	1.4(-6)	120	5.6(-6)	117
(CH ₃) ₂ CO	3.5(-13)	74	2.9(-11)	72	2.1(-10)	66
CH ₃ CONH ₂	4.0(-11)	124	2.7(-10)	120	5.0(-9)	117
CH ₃ COOH	3.0(-12)	124	4.7(-11)	120	2.4(-9)	117
CH ₃ OCOCH ₃	4.6(-14)	104	1.0(-12)	97	3.9(-11)	94
CH ₂ (OH)COCH ₃	3.0(-13)	124	5.7(-12)	120	3.1(-10)	117
(CH ₃ O) ₂	4.8(-10)	111	1.4(-9)	108	1.5(-9)	98
(CH ₂ OH) ₂	1.4(-8)	159	1.5(-8)	171	1.9(-8)	175
CH ₃ OCH ₂ OH	4.8(-9)	133	1.8(-8)	125	4.0(-8)	119
CH ₃ ONH ₂	2.8(-8)	127	1.2(-7)	123	4.3(-7)	119
CH ₂ (OH)NH ₂	3.3(-8)	124	1.9(-7)	143	4.5(-7)	143

Table 4—Continued

Species	Model F		Model M		Model S	
	Peak $n[i]/n_H$	T (K)	Peak $n[i]/n_H$	T (K)	Peak $n[i]/n_H$	T (K)
CH ₃ OCO	7.0(-12)	200	4.7(-10)	200	7.3(-9)	196
CH ₂ (OH)CO	1.8(-11)	200	3.2(-10)	200	7.3(-9)	200
(CH ₃ O) ₂ CO	1.1(-12)	130	1.2(-11)	125	1.4(-10)	122
(CH ₂ OH) ₂ CO	1.7(-11)	166	9.7(-11)	175	1.6(-9)	179
CH ₃ OCOCH ₂ OH	8.0(-12)	130	1.2(-10)	128	1.0(-9)	119
CH ₃ OCONH ₂	6.9(-11)	124	1.4(-9)	120	1.2(-8)	117
CH ₂ (OH)CONH ₂	4.3(-10)	145	2.4(-9)	157	2.0(-8)	163
(NH ₂) ₂ CO	3.1(-9)	124	3.5(-8)	123	3.4(-7)	119
NH ₂ COCHO	9.7(-11)	124	4.7(-11)	120	2.2(-10)	117
NH ₂ COOH	5.3(-9)	124	4.4(-8)	125	1.8(-7)	122
CH ₃ OOH	2.1(-8)	119	8.3(-8)	115	2.2(-7)	109
CH ₂ (OH) ₂	5.2(-8)	124	1.9(-7)	123	5.1(-7)	117
HOCOOH	2.6(-9)	127	3.6(-8)	123	1.1(-7)	119
CH ₃ OCOOH	1.5(-10)	127	2.6(-9)	123	7.9(-9)	119
CH ₂ (OH)COOH	3.5(-10)	152	2.8(-9)	160	1.8(-8)	163
HCOCOCHO	1.5(-13)	94	1.4(-13)	89	7.4(-13)	85
CH ₃ COCHO	1.9(-12)	82	4.2(-12)	78	1.5(-11)	75
OHCCOOH	1.7(-12)	127	4.0(-12)	123	1.3(-10)	119
CH ₃ OCOCHO	1.3(-13)	116	2.5(-13)	112	5.7(-12)	109
CH ₂ (OH)COCHO	2.5(-13)	133	6.4(-13)	128	1.5(-11)	119
C ₂ H ₆	1.1(-7)	96	7.7(-7)	92	1.6(-6)	90
OHCCHO	5.5(-10)	71	1.1(-9)	68	2.1(-9)	63
H ₂ O ₂	4.1(-7)	127	9.9(-7)	123	1.6(-6)	117
(NH ₂) ₂	1.2(-7)	127	5.5(-7)	125	3.6(-6)	128
COCHO	7.9(-12)	200	1.4(-11)	200	1.9(-10)	200

[†] $a(b) = a \times 10^b$

Table 5. Selection of ice compositions determined or collated by Gibb et al. 2000, and post-collapse model values ^a

Species	W33A	NGC 7538	IRS 9 ^b	Sgr A* ^b	Standard model ^c	Reduced values ^c
CO	8	16	<12	<12	19	19
CO ₂	13	22	14	14	4.1(-3)	4.1(-3)
CH ₄	1.5	2	2	2	22	2.2
CH ₃ OH	18	5	<4	<4	15	1.5
H ₂ CO	6	4	<3	<3	4.3	0.43
HCOOH	7	3	3	3	3.2(-6)	3.2(-6)
NH ₃	15	13	20–30	20–30	25	25

^aAll values are expressed as a percentage of the H₂O value

^bSee Gibb et al. 2000 for original references

^cX(H₂O)=2.3(-4)

Table 6. Peak gas-phase abundances and associated temperatures for reduced ice composition run[†].

Species	Model F(ice)		Model M(ice)		Model S(ice)		Sgr B2(N)				
	$n[i]/n_H$	T (K)	$n[i]/n_H$	T (K)	$n[i]/n_H$	T (K)	$n[i]/n_H$	T_{rot} (K)	θ	Ref.	Notes
CO	4.4(-5)	26 ‡	4.1(-5)	25 ‡	3.4(-5)	200 ‡	1.6(-5)	50	23''	(1)	From C ¹⁷ O
H ₂ O	2.3(-4)	186	2.3(-4)	200	2.1(-4)	200	-	-	-		
CH ₄	5.0(-6)	29 ‡	5.2(-6)	29 ‡	6.1(-6)	28 ‡	-	-	-		
NH ₃	5.6(-5)	124	5.3(-5)	120	4.2(-5)	117	-	-	-		
HCO ⁺	7.0(-10)	35	6.9(-10)	61	7.7(-10)	49	1.3(-10)	50	23''	(1)	From H ¹³ CO ⁺
CH ₃ OH (early)	3.3(-10)	44	7.0(-10)	42	1.1(-9)	40	1.7(-9)	45	23''	(1)	(Halo)
CH ₃ OH (late)	3.2(-6)	119	2.6(-6)	117	1.4(-6)	112	8.3(-7)	238	2''	(1)	(Core)
H ₂ CO	1.1(-6)	42	1.5(-6)	41	1.9(-6)	40	2.5(-10)	50	23''	(1)	
HCOOH (early)	9.9(-10)	47	1.3(-9)	42	1.5(-9)	40	7.0(-11)	74 ⁺⁸² ₋₃₀	23''	(1)	
HCOOH (late)	4.6(-9)	124	4.7(-9)	120	6.3(-10)	117	1.5(-9)	74 ⁺⁸² ₋₃₀	5''	(1)	Scaled from 23'' data
HCOOCH ₃	7.8(-11)	84	1.0(-10)	80	4.5(-10)	78	1.9(-8)		14'' × 4''	(2,3)	(BIMA data)
CH ₃ OCH ₃	3.0(-9)	200	6.3(-9)	200	4.2(-9)	149	1.3(-9)	197 ⁺³¹ ₋₂₂	23''	(1)	
CH ₂ (OH)CHO	8.8(-11)	124	1.7(-10)	120	3.1(-10)	117	4.7(-11)	50	> 1'	(4)	
C ₂ H ₅ OH	1.5(-9)	124	3.8(-9)	120	7.3(-9)	117	7.0(-10)	8	55''	(4)	
							73 ⁺⁵ ₋₄	73 ⁺⁵ ₋₄	23''	(1)	
							1.5(-8)	73 ⁺⁵ ₋₄	5''	(1)	Scaled from 23'' data
CH ₃ CHO (early)	2.8(-12)	57	1.5(-10)	54	3.8(-10)	52	7.3(-11)	59 ⁺²² ₋₁₃	23''	(1)	(a-type)
CH ₃ CHO (late)	2.4(-11)	200	1.9(-10)	200	1.7(-9)	125	5.3(-9)	520 ⁺¹⁰⁴⁰ ₋₂₂₀	23''	(1)	(b-type)
							1.1(-7)	520 ⁺¹⁰⁴⁰ ₋₂₂₀	5''	(1)	(b-type) Scaled from 23'' data
CH ₂ CO	2.0(-9)	46	5.8(-9)	45	7.6(-9)	42	1.2(-10)	120 ⁺⁶⁸ ₋₃₄	23''	(1)	
CH ₃ CN	2.0(-9)	96	6.8(-9)	94	1.2(-8)	103	1.1(-7)	400 ⁺¹⁰⁴ ₋₈₆	2.7''	(1)	(Filling factor assumed)
							3.1(-8)	400 ⁺¹⁰⁴ ₋₈₆	5''	(1)	Scaled from 2.7'' data
HCN (early)	2.3(-8)	51	5.9(-8)	44	1.9(-7)	41	4.2(-10)	50	23''	(1)	From HC ¹⁵ N
HCN (late)	2.1(-8)	200	6.8(-8)	200	1.7(-7)	200	9.0(-9)	50	5''	(1)	Scaled from 23'' data
HNCO	3.4(-11)	200	1.1(-9)	200	1.2(-8)	163	2.8(-10)	212 ⁺⁴⁶ ₋₃₄	23''	(1)	
							6.0(-9)	212 ⁺⁴⁶ ₋₃₄	5''	(1)	Scaled from 23'' data
NH ₂ CHO (early)	3.0(-10)	45	3.6(-10)	41	4.3(-10)	41	9.3(-11)	175 ⁺⁵³ ₋₃₈	23''	(1)	(a-type)
							2.0(-9)	175 ⁺⁵³ ₋₃₈	5''	(1)	(a-type) Scaled from 23'' data
NH ₂ CHO (late)	1.0(-7)	200	1.9(-7)	200	1.4(-7)	136	1.6(-9)	302 ⁺¹²⁶ ₋₇₅	23''	(1)	(b-type)
							3.3(-8)	302 ⁺¹²⁶ ₋₇₅	5''	(1)	(b-type) Scaled from 23'' data
CH ₃ NH ₂	1.1(-7)	124	2.6(-7)	120	1.8(-7)	117	2.5(-6)	230 ⁺⁷⁴ ₋₄₆	1.1''	(1)	(Filling factor assumed)
NH ₂ OH	3.5(-7)	122	1.2(-6)	120	4.2(-6)	114	-	-	-		
(CH ₃ O) ₂	6.3(-12)	109	1.4(-11)	105	1.2(-11)	96	-	-	-		
(CH ₂ OH) ₂	3.6(-11)	166	9.6(-11)	171	3.2(-10)	175	3.3(-10)	200	84''	(5)	

Table 6—Continued

Species	Model F(ice)		Model M(ice)		Model S(ice)		Sgr B2(N)				
	$n[i]/n_H$	T (K)	$n[i]/n_H$	T (K)	$n[i]/n_H$	T (K)	$n[i]/n_H$	T_{rot} (K)	θ	Ref.	Notes
							9.3(-8)	200	5''	(5)	Scaled from 84'' data
							5.3(-11)	50	84''	(5)	
CH ₃ OCH ₂ OH	6.0(-11)	127	2.5(-10)	123	1.0(-9)	119	-	-	-		
CH ₃ ONH ₂	3.7(-9)	124	1.6(-8)	123	6.4(-8)	117	-	-	-		
CH ₂ (OH)NH ₂	6.4(-9)	148	2.4(-8)	147	6.8(-8)	146	-	-	-		
(CH ₃) ₂ CO	1.7(-13)	71	1.9(-12)	69	9.5(-12)	66	4.9(-9)	170	12''.5 × 5''.4	(2)	(BIMA data)
CH ₃ CONH ₂	4.3(-10)	122	2.2(-9)	120	2.0(-9)	114	3.0(-11)	8	Various	(6)	
CH ₃ COOH	4.9(-12)	122	9.3(-11)	120	7.9(-10)	114	1.0(-9)		11'' × 4''	(2,7)	(BIMA data)
CH ₃ OCOCH ₃	3.4(-14)	98	4.0(-13)	94	1.0(-12)	90	-	-	-		
CH ₂ (OH)COCH ₃	1.4(-13)	122	3.2(-12)	120	2.2(-11)	114	-	-	-		
CH ₃ OCO	9.0(-13)	200	3.6(-11)	200	4.6(-10)	183	-	-	-		
CH ₂ (OH)CO	5.0(-13)	200	1.7(-11)	200	6.0(-10)	200	-	-	-		
(CH ₃ O) ₂ CO	6.5(-15)	130	1.9(-13)	125	2.9(-12)	122	-	-	-		
(CH ₂ OH) ₂ CO	1.3(-14)	170	4.0(-13)	175	2.0(-11)	179	<8.3(-12)		33''	(8)	
CH ₃ OCOCH ₂ OH	2.6(-14)	127	5.7(-13)	123	2.2(-11)	117	-	-	-		
CH ₃ OCONH ₂	1.2(-11)	124	1.4(-10)	120	8.5(-10)	117	-	-	-		
CH ₂ (OH)CONH ₂	1.2(-11)	152	1.4(-10)	157	1.8(-9)	160	-	-	-		
(NH ₂) ₂ CO	1.5(-9)	124	1.5(-8)	123	7.3(-8)	119	-	-	-		
NH ₂ COCHO	2.4(-11)	124	8.4(-11)	120	3.4(-10)	117	-	-	-		
NH ₂ COOH	1.5(-9)	127	1.2(-8)	123	8.9(-8)	119	-	-	-		
CH ₃ OOH	2.1(-9)	116	6.5(-9)	115	1.9(-8)	109	-	-	-		
CH ₂ (OH) ₂	5.5(-9)	124	1.9(-8)	120	6.8(-8)	117	-	-	-		
HOCOOH	6.5(-10)	124	4.0(-9)	123	3.6(-8)	117	-	-	-		
CH ₃ OCOOH	3.8(-12)	124	5.1(-11)	123	6.3(-10)	117	-	-	-		
CH ₂ (OH)COOH	6.9(-12)	155	7.0(-11)	160	1.8(-9)	117	-	-	-		
HCOCOCHO	5.8(-15)	90	1.7(-14)	87	6.9(-13)	83	-	-	-		
CH ₃ COCHO	1.1(-13)	79	3.1(-13)	76	2.8(-12)	75	-	-	-		
OHCCOOH	4.2(-13)	127	5.7(-12)	123	1.6(-10)	119	-	-	-		
CH ₃ OCOCHO	4.2(-15)	116	5.8(-14)	112	9.8(-13)	107	-	-	-		
CH ₂ (OH)COCHO	7.0(-15)	130	1.3(-13)	123	3.6(-12)	119	-	-	-		
C ₂ H ₆	1.4(-8)	94	5.2(-8)	92	1.6(-7)	88	-	-	-		
OHCCCHO	1.9(-11)	67	4.4(-11)	65	8.0(-10)	62	-	-	-		
H ₂ O ₂	4.2(-7)	127	5.6(-7)	123	8.5(-7)	117	-	-	-		
(NH ₂) ₂	2.2(-7)	130	1.1(-6)	128	4.9(-6)	128	-	-	-		

Table 6—Continued

Species	Model F(ice)		Model M(ice)		Model S(ice)		Sgr B2(N)			Ref.	Notes
	$n[i]/n_H$	T (K)	$n[i]/n_H$	T (K)	$n[i]/n_H$	T (K)	$n[i]/n_H$	T_{rot} (K)	θ		
COCHO	1.9(-12)	200	2.3(-11)	200	2.5(-10)	191	-	-	-		

$\dagger a(b) = a \times 10^b$

\ddagger Modeled abundance values for CO and CH₄ are largely constant over a wide range of temperatures.

Note. — Bracketed comments in the ‘notes’ column derive from the original reference. Iostopic ratios C¹²/C¹³=70, O¹⁶/O¹⁷=2044, and N¹⁴/N¹⁵=100 are assumed.

References. — (1) Nummelin et al. 2000; (2) Snyder et al. 2002 (3) Liu, Mehringer & Snyder 2001; (4) Hollis et al. 2004; (5) Hollis et al. 2002; (6) Hollis et al. 2006 (7) Remijan et al. 2002 (8) Apponi et al. 2006